

# Impact of the wind field at the complex terrain site Perdigão on the surface pressure fluctuations of a wind turbine

Florian Wenz<sup>1</sup>, Judith Langner<sup>2</sup>, Thorsten Lutz<sup>1</sup>, and Ewald Krämer<sup>1</sup>

<sup>1</sup>University of Stuttgart, Institute of Aerodynamics and Gas Dynamics (IAG), Pfaffenwaldring 21, 70569 Stuttgart, Germany

<sup>2</sup>~~WRD-Management-Support-GmbH, Customer-Support~~ Wobben Research and Development GmbH, Site Analytics and Meteorology, Teerhof 59, 28199 Bremen, Germany

**Correspondence:** Florian Wenz (florian.wenz@iag.uni-stuttgart.de)

**Abstract.** ~~The influence of turbulent inflow, as it occurs in complex terrain, on the unsteady surface pressure distributions on a wind turbine is investigated numerically. A method is presented that enables an accurate reproduction of the inflow to the turbine in the complex terrain in Perdigão, Portugal. For this purpose, a precursor simulation with the steady-state atmospheric computational fluid dynamics (CFD) code *E-Wind* and a high-resolution Delayed Detached Eddy Simulation (DDES) with *FLOWer* is performed. The conservation of the flow field is validated by a comparison with measurements from the 2017 field campaign in Perdigão. Then, the resolved fluid-structure coupled generic wind turbine I82 is included in the *FLOWer* simulation to investigate the impact of the complex terrain inflow on the surface pressure fluctuations on tower and blades. A comparison with simulations of the same turbine in flat terrain with simpler inflows shows that the turbine in complex terrain has a significantly different vortex shedding at the tower, which dominates the periodic pressure fluctuations at the tower sides and back. However, the dominant source of periodic pressure fluctuations on the upper part of the tower, the blade-tower interaction, is hardly altered by the terrain flow. The pressure fluctuations on the blade have a rather broadband characteristic, caused by the interaction of the leading edge with the inflow turbulence. In general, it is shown that a sophisticated DDES of the complex terrain plays a decisive role in the unsteady aerodynamics of the turbine, due to its specific flow characteristic.~~

**R3:G1-a** The surface pressure fluctuations, which are a source of low-frequency noise emissions, are numerically investigated on a 2 MW wind turbine under different inflow conditions. In order to evaluate the impact of a complex terrain flow, a computational setup is presented that is aimed at reproducing a realistic flow field in the complex terrain in Perdigão, Portugal. A precursor simulation with the steady-state atmospheric computational fluid dynamics (CFD) code *E-Wind* is used, which was calibrated with met mast data to generate a site- and situation-specific inflow for a high-resolution Delayed Detached Eddy Simulation (DDES) with *FLOWer*. A validation with lidar and met mast data reveals a good agreement of the flow field in the vicinity of the turbine. The geometrically resolved turbine is coupled to the structural solver *SIMPACK* and simulated both in the complex terrain and in flat terrain with simpler inflows as reference. The surface pressure fluctuations are evaluated on tower and blades. It is found that the periodic pressure fluctuations at the tower sides and back are dominated by vortex shedding, which strongly depends on the inflow and is reduced by inflow turbulence. However, the dominant pressure fluctuations on the upper part of the tower, which are caused by the blade-tower interaction, remain almost unchanged by the different inflows. The predominant pressure fluctuations on the blades occur with the rotation frequency. They are caused by a combination of rotor

tilt, vertical wind shear and inclined flow and are thus strongly dependent on the inflow and the surrounding terrain. The inflow turbulence masks fluctuations at higher harmonics of the blade-tower interaction with its broadband characteristic caused by the interaction of the leading edge and the inflow turbulence.

## 1 Introduction

30 In the course of the onshore expansion of wind energy, more and more wind turbines are erected in complex terrain. The disturbances of the inflow angle, the strong turbulences and the inhomogeneity of the wind field ~~that occur there~~ pose a challenge for the prediction of turbine loads, performance and noise emission. Especially the low-frequency acoustic emissions are controversially discussed in the context of public acceptance of wind turbines in onshore wind parks. The basis for an accurate prediction of acoustic low-frequency emissions is the correct simulation and understanding of their aerodynamic  
35 source, namely the surface pressure fluctuations on the tower and blades (Yauwenas, 2017; Klein, 2019). These are caused by the blade-tower interaction, the inflow turbulence and the vortex shedding, all of which are affected by the surrounding terrain and its specific flow field. The increase in computational resources enables high-fidelity simulations to capture more and more of these aerodynamic interactions in a complex terrain site and to evaluate the corresponding phenomena.

### 1.1 Numerical approaches for complex terrain and wind turbine simulations

40 Reliable methods for predicting flow characteristics are of great importance for profound site assessment, especially in complex terrain. Flow over hills is accelerated, can cause recirculation regions and turbulence characteristics are altered, all of which have been studied in research for decades, as the overview of Belcher and Hunt (1998) shows. These effects hold positive potential in terms of wind turbine performance, but also bear risks. In industry, computationally cheap approaches, such as steady-state Reynolds-averaged Navier–Stokes (RANS) simulations (Alletto et al., 2018), are ~~needed~~ **used** for assessing  
45 risky turbine position in complex terrain. ~~Large-scale meteorological effects are often captured by Large Eddy Simulations (LES) with meteorological codes such as the Weather Research and Forecasting (WRF) model, which only coarsely resolve site-specific terrain features~~ **R3:S1-a** Large-scale and long-term meteorological effects can be captured with the Weather Research and Forecasting (WRF) model, which allows the nesting of Large Eddy Simulations (LES) at the expense of only  
50 coarsely resolved topographic terrain features, such as in Wagner et al. (2019). To capture the unsteady effects occurring in the atmospheric boundary layer **(ABL)** and their interaction with complex terrain, unsteady RANS (URANS) simulations, as in Koblitz (2013), can be used. If the focus is on resolving the ~~boundary layer~~ **ABL** or on the aerodynamic interaction of the inflow  
55 ~~with~~ **and** the turbine, hybrid RANS/LES models are necessary, since the small-scale vortices must be resolved. Bechmann and Sørensen (2010) simulated the flow over a hill with a hybrid formulation similar to the Detached Eddy Simulation (DES) with good results especially for the turbulence level. Schulz et al. (2016) conducted Delayed Detached Eddy Simulations (DDES) to evaluated the effect of complex terrain on the performance of a wind turbine, and the general suitability of DDES for detailed investigations of wind turbine aerodynamics is demonstrated by Weihing et al. (2018). Sørensen and Schreck (2014) performed DDES and URANS simulations of the NREL Phase-VI rotor and found that although DDES does not improve the quality of

the mean power prediction, it significantly increases the accuracy of the predicted load spectra compared to URANS. For the overall objective **R2:G3-f** of the present paper, the investigation of surface pressure fluctuations under complex inflow conditions of investigating low-frequency acoustic emissions, which are strongly dependent on unsteady loads, it is therefore highly advisable to use DDES.

## 1.2 The complex terrain site Perdigão

A widely studied complex terrain site in the field of wind energy is the double ridge in Perdigão in central Portugal. The site consists of two parallel, well-exposed ridges, each overlooking the surrounding area by about 300m. A single wind turbine has been erected is located on the southwestern ridge. A detailed description of the orography and vegetation at the site can be found in Vasiljević et al. (2017). During the 2017 field campaign in Perdigão, a comprehensive set of measurement data of the flow over the complex terrain as well as and of the behaviour of the wind turbine within it was collected. The measurement equipment used ranges from met includes meteorological (met) masts, to lidars and microphones (Fernando et al., 2019). This campaign was is part of the New European Wind Atlas (NEWA) (Mann et al., 2017) funded by the European Union, which provides maps of wind statistics in complex terrains that can be used as a benchmark for site assessment. The NEWA experiments consist of five measurement campaigns at complex sites, of which Perdigão was the most extensive, and provide, among other things, detailed microscale validation data for simulations. In order to obtain accurate simulation results, the terrain model on which the computational fluid dynamics (CFD) simulations are based must be correspondingly detailed. Therefore, Palma et al. (2020) created a detailed digital terrain model (DTM) with a resolution of 2m, which includes orography and vegetation.

In many studies, simulations of the flow field in Perdigão have already been carried out to investigate the effects of orography, vegetation, thermal stratification as well as and meteorological effects in general. Wagner et al. (2019) performed nested LES with WRF WRF-LES for the Iberian Peninsula with a highest resolution of 200m around Perdigão covering almost 50 days. They showed that the southwest wind during the day experiences a clockwise wind turning and that the frequent nocturnal low-level jets over the double ridge from northeast already develop in Spain. Coupled WRF and URANS simulations were used by Olsen (2018) to include changing weather patterns as well as local orographic and surface effects. Characteristic eddy-structures behind the ridges were observed and with a finest mesh resolution of 80m the mean wind speed was captured well. Steady-state RANS calculations were used by Palma et al. (2020) to discuss the impact of the resolution of the terrain model as well as of the CFD mesh on the local flow. They found that the flow in the valley was most affected by the resolution and recommend a resolution below 40m. Salim Dar et al. (2019) performed LES of the double ridge in Perdigão with a resolution of 10m including the wind turbine, being represented with an actuator-disc model. They investigated the wake behaviour and found that the shape of the velocity deficit profile is preserved in downstream direction even in complex terrain, which is known as self-similarity. In addition, they found that the streamwise velocity at hub height varies with the change in terrain characteristics caused by a change in resolution. More detailed-s Simulations of the interaction between turbulent terrain flow and local wind turbine aerodynamics using a fully resolved turbine in Perdigão have not been published to the authors' knowledge.

### 1.3 Scope and objectives

The influence of terrain flow on the unsteady pressure distributions on the turbine surface is investigated in order to examine the mechanisms of low-frequency noise generation in complex terrain using the example of the double ridge in Perdigão. A method is presented that aims to enable an accurate reproduction of the inflow to the turbine in complex terrain. For this purpose, an interface is created from the atmospheric CFD code *E-Wind* to the high-resolution DDES with *FLOWer* in order to provide an unsteady wind field at the domain inlet for it. The conservation of the flow field is evaluated by means of mean velocities and turbulence statistics and validated by a comparison with measurements in Perdigão. Furthermore, the necessary properties of a numerical setup including vegetation for a numerically stable and high-quality DDES of the complex terrain are given.

Then, the fluid-structure coupled generic turbine I82 with aero-servo-elastic similarity to the actual turbine at the site is included in the *FLOWer* simulation. The resulting aerodynamic effects, in particular the unsteady pressure distributions on tower and blade, are investigated. The observations are compared with the results of DDES of the same turbine in flat terrain with uniform inflow as well as a turbulent inflow generated from *E-Wind* results at the turbine position. In this way it can be assessed whether the sophisticated DDES of the complex terrain plays a decisive role in the unsteady aerodynamics of the turbine.

**R2:G1-a** **R3:G1-b** The aim of the present paper is to numerically investigate the influence of the flow in the complex terrain in Perdigão on the unsteady pressure distributions on the turbine surface, which are a source of low-frequency noise emissions. For this purpose, a fluid-structure coupled DDES of the fully resolved 2MW wind turbine in the complex terrain of Perdigão including forest and turbulent inflow is conducted with the CFD solver *FLOWer*. A measured flow situation is reproduced by using data from a precursor simulation with the atmospheric CFD code *E-Wind*, which was calibrated with met mast data, as inflow for *FLOWer*. In a first step, the simulated terrain flow (without turbine) is validated by a comparison with measurements in Perdigão to prove the quality and suitability of the process chain for the detailed simulation of the wind field in the complex terrain. Then, the wind turbine is included in the fluid-structure coupled *FLOWer* simulation, and the turbine wake, the global loads and the deformations are checked for plausibility. Finally, the unsteady pressure distributions on the tower and blades are investigated in detail, focusing on the influence of the inflow on the interaction between blades and tower as well as on the vortex shedding at the tower. The observations are compared with the results of DDES of the same turbine in flat terrain both with uniform and turbulent inflow to highlight peculiarities.

## 2 Numerical tools

The high-fidelity process chain for the calculation of unsteady aerodynamics under site- and situation-specific inflow in complex terrain comprises several solvers. The atmospheric steady-state CFD RANS solver *E-Wind* for the simulation of the Perdigão site provides the inflow conditions for unsteady high-resolution DDES of the turbine near-field with the CFD solver *FLOWer*. The geometrically resolved turbine can be included in this simulation and a time-accurate coupling to the structural solver *SIMPACT* enables the consideration of aeroelastic effects caused by the fluid-structure interaction (FSI).

## 2.1 Atmospheric CFD code - E-Wind

125 *E-Wind* is an atmospheric CFD tool developed and used by Enercon for wind resource assessment (Alletto et al., 2018). *E-Wind* solves the steady -state RANS equations using the  $k - \varepsilon$  turbulence model **R3:S8-a**, where the turbulent kinetic energy  $k$  and **R3:S9-a** the rate of dissipation  $\varepsilon$  are the two transported variables. The governing equations are adapted to atmospheric ABL conditions, e.g. complex terrain, roughness and forest (vegetation), atmospheric stability and Coriolis force (Sogachev et al., 2012) and solved using the open source code OpenFOAM (v1712) as the core solver within *E-Wind*. Since the exact boundary  
130 condition (BC) for ground roughness and thermal stability are often unknown, the roughness scaling factor ( $RSF$ ) and heat flux ( $HF$ ) are used to calibrate the simulations **R3:S2-a** a scaling of the roughness map and the ground heat flux can be used in a calibration process against mast measurements to fit match the **R3:S7-a** vertical wind shear at the met mast location. For a detailed description of the calibration process see Adib et al. (2021).

## 2.2 Unsteady CFD solver - FLOWer

135 The basis for the numerical simulations of the wind turbine is the CFD solver *FLOWer*, which was originally developed by the German Aerospace Center (DLR) (Kroll et al., 2000). It is a compressible, block structured RANS solver. The numerical scheme is based on a finite-volume formulation. The implemented Chimera technique allows the use of independent grids for the individual components of the wind turbine and the background. The solver has been continuously extended at the authors' institute to improve its suitability for wind turbine simulations. Among others, the fifth-order weighted essentially non-oscillatory scheme WENO is available for spatial discretization (Kowarsch et al., 2013) and several hybrid RANS/LES schemes  
140 have been implemented in *FLOWer* (Weihsing et al., 2018). Furthermore, a body forces approach is included to superimpose atmospheric turbulence on the inflow (Schulz et al., 2016) and forest regions are accounted for by volume forces added to the momentum equation of the Navier-Stokes equations (Letzgus et al., 2018). The work of Klein et al. (2018) introduced a revised coupling to the multi-body simulation tool *SIMPACK*.

## 145 2.3 Structural solver - SIMPACK

*SIMPACK* is a commercial software for the simulation of multi-body systems. The dynamic systems can consist of rigid and flexible bodies connected by joint elements. The flexible turbine components such as the tower and blades can be modelled either as beams or as modal bodies by reading in the modal properties. External forces such as aerodynamic forces can be defined internally or imported from other programs via a predefined interface environment. Controllers can also be integrated.  
150 *SIMPACK* has recently been used by industrial and research groups for the simulation of wind turbines, e.g. Luhmann et al. (2017) and Guma et al. (2021).

### 3 Computational setup

~~The complex terrain in Perdigão with its double ridge was simulated without and with a turbine on site. In addition, two reference simulations were conducted in *FLOWer* with the same turbine in flat terrain.~~

155 The setup of the complex terrain simulation aimed ~~s~~ to reproduce a measured flow situation R2:G2-a to allow for a validation of the local wind field simulated with *FLOWer*. The situation ~~was~~ **is** selected based on operating data from the turbine in Perdigão, with the objective of having fairly constant operating conditions close to ~~the~~ rated conditions. This ~~was~~ **is** found to be the case for a thirty-minute interval on 10 May 2017 from 15:15:00 UTC with an inflow from southwest ( $230^\circ$ ). The measured data ~~was~~ **is** averaged over this interval ~~before serving as a reference.~~

#### 160 3.1 Atmospheric precursor simulation with E-Wind

~~*E-Wind* provides a site- and situation-specific mean flow field, as it is calibrated with mast measurements on the real site in Perdigão. The equations in *E-Wind* were discretised using a mixed 1st/2nd order scheme.~~ R2:G2-b *E-Wind* is used to extrapolate a site- and situation-specific mean flow field from the measured wind profile at a met mast location. This provides a prediction of the flow conditions at any other location at the site, including the position where the *FLOWer* domain inlet is placed and where no measurement data is available. Thus, the necessary *FLOWer* inflow conditions can be extracted from the modelled flow field. Due to the high resolution and up to date terrain and forest maps, no roughness calibration ~~was~~ **is** performed ( $RSF=1$ ) R3:S2-b. For the selected situation, good calibration results ~~could~~ **can** be obtained for met mast 20 under neutral thermal conditions ( $HF=0$ ) R3:S2-c ~~no ground heat flux~~. ~~The equations in *E-Wind* are discretized using a mixed 1st/2nd order scheme~~ (Alletto et al., 2018). ~~The convergence criteria of the simulation for the velocity and  $k$  are reached after about 2200 iterations.~~

165  
170

##### 3.1.1 Mesh and boundary conditions for E-Wind

*E-Wind* uses a cylindrical domain with a diameter of 22.5 km and a height of 6 km (see Fig. 1). The Perdigão terrain mesh in *E-Wind* ~~was~~ **is** based on the high-resolution (2m) map provided by Palma et al. (2020). It ~~was~~ **is** resampled to a resolution of 10m to fit the mesh resolution and to avoid artefacts in the mesh. Since the scanned area is smaller than the computational domain, the map ~~was~~ **is** extended with data from the Shuttle Radar Topography Mission (SRTM). The coordinate system used for both the maps and the domain is ETRS89 / Portugal TM06 (EPSG:3763). To allow for homogeneous inflow, the terrain ~~was~~ **is** flattened towards the lateral boundaries by a 3km wide ramp followed by a 2km wide flat area.

175

The structured mesh for *E-Wind* ~~with~~ **has** about 9.4 million cells ~~was created with *Pointwise*~~. A fine grid with 10m horizontal resolution and 1m vertical resolution is used in the centre of the domain, which is coarsened towards the lateral and upper boundaries. At a height of 500m above the highest terrain elevation, the horizontal resolution is doubled to 20m. The mesh is aligned with the wind direction at hub height of  $WD_{hub} = 230^\circ$ . The ground surface is modelled as no-slip wall, using wall functions for the turbulent quantities and a fixed heat flux for the temperature. For the upper boundary, slip conditions for velocity, temperature,  $k$  and  $\varepsilon$  are applied, while the pressure gradient is fixed to prescribe the geostrophic forcing. At the sides

180

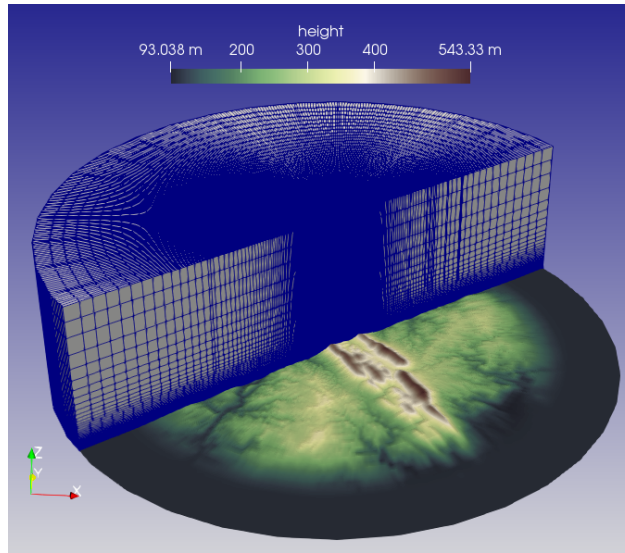


**Figure 1.** Mesh of *E-Wind* for a wind direction of  $230^\circ$  (inflow parallel to cutting plane).

of the domain, an *inletOutlet* boundary-condition **R3:S2-d** **OpenFOAM BC** is used with a precomputed profile for the inflow  
 185 and a zero gradient condition for the outflow. For more details, see Alletto et al. (2018). The geostrophic wind speed was is  
 set to  $11 \text{ ms}^{-1}$  and the geostrophic wind direction to  $242^\circ$ .

### 3.1.2 Vegetation in E-Wind

To account for vegetation in *E-Wind*, a map of the roughness length  $z_0$  must be provided, which is then applied as either  
 roughness or as forest depending on the actual  $z_0$  value. The provided forest height map with 2 m resolution (Palma et al.,  
 190 2020) was is also resampled to 10 m and smoothed with a Gaussian filter. The forest height was is divided by the forest scaling  
 factor  $FSF = 10$  to derive the  $z_0$  map. The calculated  $z_0$  values were are then classified into eight different classes. The  
 forest model described in Alletto et al. (2018) was is applied for  $z_0 > 0.5 \text{ m}$ , which applies to the three highest  $z_0$  classes. The  
 constant leaf area density  $LAD = 0.2$ , the drag coefficient  $c_d = 0.15$  and the forest height  $h = FSF \cdot z_0$  were are used. The  
 lower five classes are treated as roughness with a wall function (**R3:S2-e** **OpenFOAM BC** *nutkAtmRoughWallFunction*). A  
 195 constant value of  $z_0 = 1.0 \text{ m}$  is used outside of the provided map, representing forest with  $h = 10 \text{ m}$ .

### 3.2 Complex Unsteady terrain simulation with FLOWer

The high-resolution unsteady simulations with *FLOWer* were are carried out as DDES (Spalart et al., 2006) based on the  
 Menter SST  $k - \omega$  RANS model (Gritskevich et al., 2013) **R2:G2-c**, following the literature mentioned in Sect. 1.1. The  
 flow was is considered to be fully turbulent. An implicit second-order dual time-stepping scheme was is deployed for time  
 200 integration. The second-order Jameson-Schmidt-Turkel (JST) scheme was is used for the spatial discretization in the boundary

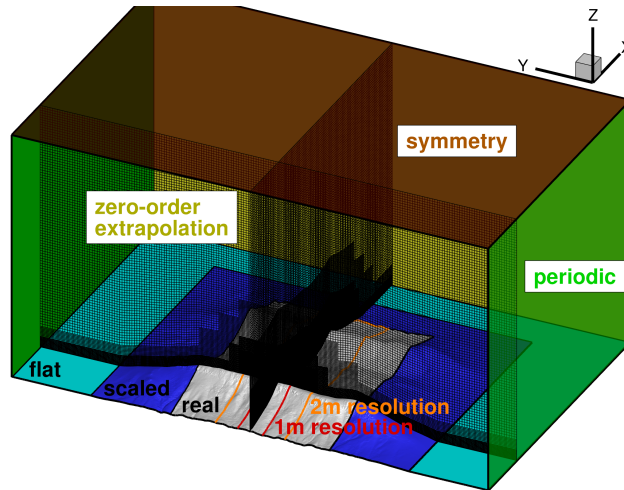


**Figure 2.** CFD domain for the *FLOWer* simulation of the complex terrain in Perdigão with boundary conditions and terrain mesh for a wind direction of  $230^\circ$ .

layer (BL) cells and the fifth-order WENO scheme **was is** applied to the Perdigão terrain mesh to reduce the dissipation of vortices. A physical time step corresponding to  $\Delta t \approx 0.5\Delta_0/u_{hub}$  **was is** used, where  $\Delta_0$  is the smallest grid size and  $u_{hub}$  is the **horizontal** flow velocity at the turbine position at hub height from *E-Wind*. The dual-time stepping scheme used **s** 80 inner iterations, which decreased **s** the global root-mean-square density residual by two orders of magnitude. To dissipate pressure and density disturbances caused by the enforced velocity profiles of the Dirichlet **boundary-condition BC** at the inlet and to obtain an initialisation of the mean velocity field, a pre-run with an increased time step ( $\approx 70 \cdot \Delta t$ ) **was is** utilized.

### 3.2.1 Terrain mesh and boundary conditions for FLOWer

Basis of the Perdigão terrain mesh for *FLOWer* is the same highly resolved (2m resolution) **digital-terrain-model-(DTM)** of the site in Perdigão (Palma et al., 2020) as for *E-Wind* (without resampling). This DTM **was is** shifted so that the tower base of the turbine is located at  $x = y = 0$  and **rotated to align** the  $x$ -axis **was rotated to align** with **the horizontal wind direction**  $W D_{hub} = 230^\circ$  **at the turbine position at hub height**. To reduce the impact of the domain boundary **ies** on the flow field in the region of interest, they **were are** placed far away ( $-768\text{m} < x < 3072\text{m}$ ,  $-3072\text{m} < y < 3072\text{m}$ ) **as visualized in Fig. 2**. **In addition, the terrain was manipulated in the direction of the lateral boundaries and outlet to have a flat bottom, as visualized in Fig. 2.** **R3:S5-a** **In addition, the DTM is smoothed at the lateral and rear boundaries (dark blue area) to blend into a flat bottom** (light blue area), while it remains unchanged in the region of interest (grey are). This allows periodic **boundary-conditions-(BC)** **BCs** to be used laterally and, due to the associated reduced flow gradients, problems with numerical stability can be avoided. The domain inlet **was is** placed at the base of the first ridge and **was is** carried out as Dirichlet BC. The domain extends vertically up to  $z = 3447\text{m}$ . The simulated area above the ground is thus about ten times the maximum height difference of the terrain, which allows for a symmetry BC at the top (Koblitz, 2013). A zero-order extrapolation **was is** applied at the outlet.

220 The Perdigão terrain mesh **was is shown in Fig. 2. It is** created using cubic cells with a resolution of  $\Delta_0 = 1$  m around the turbine and its direct inflow ( $-768\text{ m} < x < 512\text{ m}$ ,  $-160\text{ m} < y < 160\text{ m}$ ,  $z < 256\text{ m}$  a.g.l. **R3:S5-b**, marked with red lines). The cells are slightly stretched **and or** squeezed in  $z$ -direction and skewed to follow the terrain. This resolution is sufficient to resolve the ambient turbulence with an integral length scale  $L > 20\Delta_0 = 20\text{ m}$ , following Kim et al. (2016). This region **of interest** is embedded in a band ( $y = \pm 448\text{ m}$ ) with 2 m resolution that covers both ridges **and resolves detailed terrain features**

225 (see **R3:S5-c** marked with orange lines in Fig. 2). A coarsening of the mesh towards the domain boundaries **was is** applied using hanging grid nodes to reduce the number of cells and to dissipate the turbulence towards the **boundary-conditions BCs** for stability reasons. Close to the ground (no-slip wall-**BC**), BL cells with reduced resolution in  $z$ -direction (growth rate of 1.12) **were are** included to ensure  $y^+ < 5$  in the region of interest. This is crucial since without BL cells the Menter SST  $k - \omega$  RANS model remains in  $k - \varepsilon$  mode even in the first wall normal cells (switch to  $k - \omega$  only for  $y^+ < 70$  (Leschziner, 2015)).

230 Moreover, the DDES shielding fails without BL cells and the modelled stresses are depleted, which can lead to grid induced separation on the ridge. Overall, the Perdigão terrain mesh consists of 242 million cells.

### 3.2.2 Vegetation in FLOWer

Menke et al. (2019b) discussed how sensitive the simulation result is with respect to the forest parametrisation. They found that the standard forest **height  $h = 30\text{ m}$**  often used in simulations ( **$h = 30\text{ m}$** ) causes too much drag. For this reason, **much**

235 **effort was put into** an accurate representation of the forest **R3:S6-a** **upstream of the turbine is targeted**. In *FLOWer* the model of Shaw and Schumann (1992) is applied, which is based on the expression

$$F_i(z) = -c_d LAD(z) |u_i| u_i. \quad (1)$$

The drag force  $F_i$  **in the direction  $i$**  depends on the two forest characteristics  $c_d$ , a constant drag coefficient, and the leaf area density profile  $LAD(z)$ . Moreover, it scales with the local flow velocity  $u_i$  squared.

240 The drag coefficient  $c_d$  **was is** set to 0.15 as proposed by Shaw and Schumann (1992). The  $LAD$  profile which characterizes the tree type **was calculated by means of the leaf area index  $LAI$  following** **R3:S3-a** **is approximated on the basis of the leaf area index  $LAI$  according to** Lalic and Mihailovic (2004).

**The leaf-area distribution can be defined as** **R3:S3-b** **They derived the empirical leaf-area density distribution function**

$$LAD(z) = LAD_m \left( \frac{h - z_m}{h - z} \right)^n \exp \left[ n \left( \frac{h - z_m}{h - z} \right) \right]$$

245 with

$$n = \begin{cases} 6 & 0 \leq z < z_m \\ 0.5 & z_m \leq z \leq h \end{cases} \quad (2)$$

where  $h$  is the tree height and  $LAD_m$  the maximum value of  $LAD$  at the corresponding height  $z_m$ .

The tree height  $h$  and the leaf-area index  $LAI$  are included in the available maps for the site in Perdigão (Palma et al., 2020). The tree types growing in Perdigão are eucalyptus and pines (Mann et al., 2017). Lalic and Mihailovic (2004) show

**Table 1.** **R3:S4-b** Tree height  $h$ , Leaf-area index  $LAI$ , maximal leaf-area density  $LAD_m$  and corresponding height  $z_m$  for each forest patch.

$h$ [m]	$LAI$	$LAD_m$ [ $\text{m}^2\text{m}^{-3}$ ]	$z_m$ [m]	patch colour
8	2.59	0.56	4.8	cyan
11	2.93	0.46	6.6	dark green
12	2.10	0.30	7.2	light green
14	2.44	0.30	8.4	yellow
18	3.31	0.32	10.8	light orange
18	3.18	0.30	10.8	dark orange

Colours refer to Fig. 3b.

250 that their model fits measured leaf-area density distributions of pine forests well with **R3:S3-d** the maximal  $LAD$  at  $z_m = 0.6h$ ;  $z_m/h = 0.6$ . This value was therefore applied in this study. The maximal leaf-area density value  $LAD_m$  could finally be calculated by inserting Eq. (2) into **R3:S3-c** With this assumption the maximal leaf-area density value  $LAD_m$  is obtained by substituting Eq. (2) into (3) and numerically solving the integral for  $LAD_m$ .

$$LAI = \int_0^h LAD(z) dz. \quad (3)$$

255 The contour plot of the tree height in the area upstream of the turbine for  $WD = 230^\circ$  in Fig. 3a shows many small clusters with different heights. The implementation of the forest model in *FLOWer* (Letzgus et al., 2018) expects separate forest meshes when the forest characteristics change in flow direction making it unsuitable for small clusters. Therefore, the small clusters were summarized **are combined** into six forest patches with different heights and  $LAD$  distributions which were included in the simulations. The chosen patches and their tree height, which is the average value over the patch, are depicted in Fig. 3b.

260 The  $LAI$  was also averaged over each forest patch and the resulting  $LAD$  distributions in Table 1 were used, respectively. **R3:S6-b** which are included in the simulation as depicted in Fig. 3b. **R3:S4-a** The lowest relevant tree height is chosen to be 8 m. All areas with a tree height within  $\pm 20\%$  of this height are binned. Then a patch is created that envelopes all collected areas. Small gaps between collected areas are closed and small, distant clusters are neglected. This process is repeated two more times with the subsequent tree height ranges ( $12\text{ m} \pm 20\%$  and  $18\text{ m} \pm 20\%$ ). The procedure allows to obtain several separate

265 patches with the same tree height if they are all large enough but too far apart to be merged. After all patches are defined, the mean tree height and the mean  $LAI$  are calculated for each of them. With Eq. (2) and (3) and  $z_m$ , the  $LAD$  distribution can be defined. The forest definition used in the simulation is summarized in Table 1.

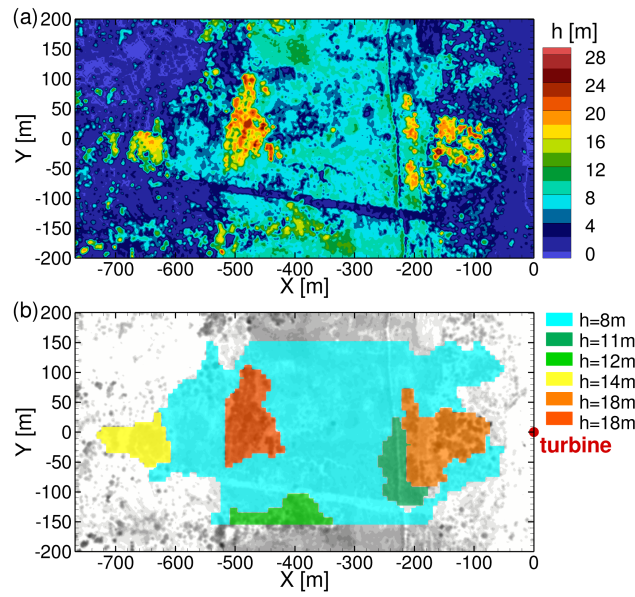


**Figure 3.** Tree height in the area upstream of the turbine for a wind direction of  $230^\circ$  (a) and forest patches included in simulation (b).

### 3.3 Atmospheric-Aerodynamics interface

The steady-state velocity profiles from *E-Wind* were passed to *FLOWer* via Dirichlet BC and the resolved synthetic turbulence based on statistical turbulence data from *E-Wind* was superimposed. From the results **R3:S10-a** steady-state flow field of the *E-Wind* simulation, a slice was is extracted at the position of the *FLOWer* domain inlet (perpendicular to  $WD = 230^\circ$ ). The three velocity components (longitudinal  $u$ , lateral  $v$  and vertical  $w$ ), the turbulence kinetic energy  $k$  as well as and **R3:S9-b** the rate of dissipation  $\epsilon$  were are averaged in lateral direction ( $\pm 100\text{m}$  relative to the turbine) for each height above ground. These values were are used to create the inflow for *FLOWer*.

Figure 4 shows the the velocity profiles of all three components above ground level (a.g.l.) **R3:S10-b** as derived from *E-Wind* (dashed lines). The profiles of all velocity components were are approximated by piecewise-defined functions **R3:S10-c** (solid lines) such that they match **R3:S10-d** resemble the results of *E-Wind* **R3:S10-e** at the lower part and are constant ( $u$ ,  $v$ ) or zero ( $w$ ) towards the upper boundary. Wind shear ( $u(z)$ ), wind veer ( $v(z)$ ) and flow inclination ( $w(z)$ ) were **R3:S7-b** The functions are prescribed at the domain boundary **R3:S10-f** *FLOWer* inlet as Dirichlet BC boundary condition with the found equations. **R3:S7-c** In this way, the vertical wind shear, the vertical wind veer and the flow inclination are taken into account. The inlet of the simulation with *FLOWer* is already in the uneven terrain at the base of the first ridge (inclination  $\approx 6^\circ$ ). Therefore, it is crucial to prescribe the vertical velocity component  $w(z)$  in order not to overestimate the speed-up at the ridge by deflecting the flow too much.

The turbulence intensity  $TI$  of the inflow for the generation of synthetic turbulence was assessed from the laterally averaged *E-Wind*  $k$  values in 77m height above ground, which corresponds to the hub height, according to **R3:S8-b** The turbulence

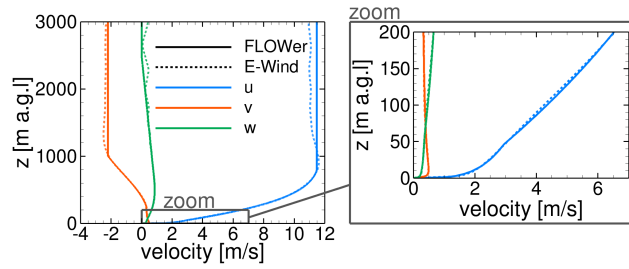


**Figure 4.** Mean velocity profiles at the *FLOWer* inlet for the entire height of the domain and zoomed to near-ground level. **E** as extracted from *E-Wind* as well as the approximation and approximated for *FLOWer* input.

intensity  $TI$  and the turbulent length scale  $L$  of the inflow are calculated from the turbulence quantities  $k$  and  $\varepsilon$  modelled in *E-wind* at 77 m a.g.l. (laterally averaged) according to

$$TI = \frac{\sqrt{\frac{2}{3}k_{z=77\text{m}}}}{\sqrt{u_{z=77\text{m}}^2 + v_{z=77\text{m}}^2}} \cdot 100\%, \quad (4)$$

with the corresponding turbulent length scale  $L$  **R3:S8-c** and

$$L = 0.09^{4/3} \frac{k_{z=77\text{m}}^{3/2}}{\varepsilon_{z=77\text{m}}}. \quad (5)$$

The resolved atmospheric turbulence for the *FLOWer* simulation was is created using Mann's model (Mann, 1994) and was is injected using a momentum source term (Troldborg et al., 2014), superimposing the steady sheared inflow **R3:S7-d** profiles at a distance of  $L$  from the inlet. To comply with the atmospheric conditions according to IEC 61400-1 (2019), an anisotropic turbulence was is generated. As recommended by Mann (1998), the stretching factor in the model was is chosen as to be 295  $\Gamma = 3.9$  to approximate the Kaimal spectral model. It was is ensured that the dimension of the Mann box is larger than  $8L$  in all directions and that its resolution is smaller than  $L/8$ .

The injection via forces as well as the numerical dissipation due to the resolution of the meshes cause a certain turbulence decay within the CFD simulation. This effect was is taken into account by applying a scaling factor  $f_{CFD} = 1.4$  on the velocity fluctuations of the Mann box, following Kim et al. (2016) for a propagation distance of approximately  $20L$ .

### 300 3.4 Turbine

The examined wind turbine is a generic 2MW turbine named I82 (Arnold et al., 2020) with aero-servo-elastic similarity to the commercial turbine at the site. The turbine has a hub height of 77 m and a rotor radius of  $R = 41$  m. The blades are pre-bended ( $-1.8$  m at the tip) and feature winglets. The rotor is mounted with a tilt angle of  $5^\circ$  and a pre-cone angle of  $0^\circ$ . The tower has a bottom diameter of  $d_b = 4.3$  m and a top diameter of  $d_t = 2.0$  m.

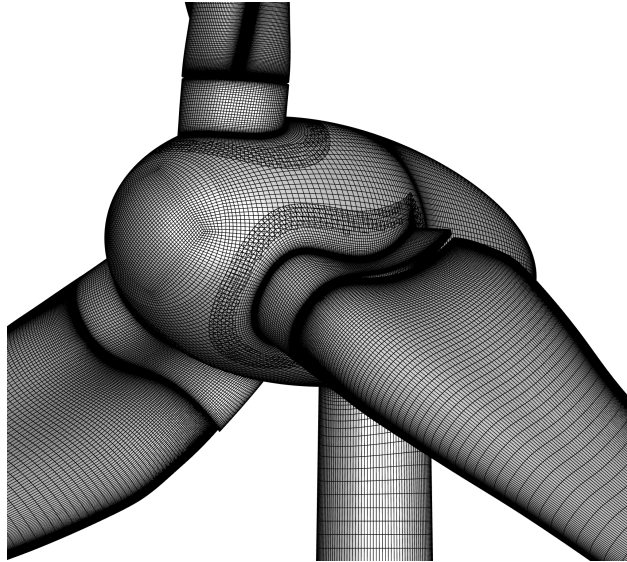


**Figure 5.** CFD surface mesh of hub region, showing mesh overlappings.

### 305 3.4.1 CFD model in FLOWer

The unsteady *FLOWer* simulations of the turbine **were are** based on the process chain established by Klein et al. (2018). The CFD model of the I82 turbine for the simulation with *FLOWer* consists of 17 independent meshes, which **were are** embedded in the Perdigão terrain mesh or a flat background mesh, respectively. Three blade tip refinements and a rotor disk refinement comprise the turbine component meshes, namely lower tower, upper tower, nacelle, hub, blade-hub connectors (3×), blades  
 310 (3×) and winglets (3×). There are no gaps between the turbine components (see Fig. 5) and the **boundary-layer BL** of all components is fully resolved ( $y^+ < 1$ ). The blades **were are** meshed in an O-topology based on the guidelines of Vassberg et al. (2008), with a special focus on a good resolution of the **boundary-layer BL** and the blade wake.

Three differently resolved blade meshes **were are** used to conduct a grid convergence study following Roache (1994) ( $y^+ < 1$  **was is** kept in all blade meshes). The conservative numerical error for the medium blade mesh ( $GCI_{coarse}^{21}$ ) is 0.4% for thrust  
 315 and 0.6% for torque. This is acceptable, and hence the blade mesh with medium resolution **was is** chosen, with 192 cells in radial direction, 304 cells around the airfoil, 64 cells on the trailing edge and 144 cells wall normal resulting in 11.4 million cells per blade. The growth rate in the **boundary-layer BL** is 1.09. The second-order JST scheme **was is** used for spatial discretization in the component meshes. The numerical settings of the complex terrain simulation **were without turbine are** kept, but the time step **was is** reduced ~~to correspond to  $1^\circ$  azimuth for evaluation.~~

320 ~~The background meshes for the reference simulations with flat terrain in *FLOWer* were approximately  $50R$  rotor radii ( $R$ ) long ( $12.5R$  upstream of the rotor plane) and were approximately  $25R$  wide and high, once with no-slip wall and BL cells and once with slip wall and no BL cells at the bottom. The overall number of cells  $N_{cells}$  per setup is given in Table 2.~~

### 3.4.2 Structural model in SIMPACK

Klein et al. (2018) **R2:G2-d** show that the blade-tower interaction, a key mechanism investigated in the following, is dominated by the blade-tower distance, which is massively reduced when the aeroelasticity of the blades is taken into account. The structural model of the I82 turbine in *SIMPACK* was **is** adopted from Arnold et al. (2020). The blades were **are** modelled as nonlinear *SIMBEAM* **R3:S2-f** beams using 29 flexible beam elements (Euler-Bernoulli Timoshenko) per blade with Rayleigh damping. The tower was **is** adjusted to a steel tower and modelled as linear *SIMBEAM* **R3:S2-g** beam by using 77 flexible beam elements (Euler-Bernoulli) with a modal damping of  $\zeta = 0.002$ . All eigenfrequencies below 15 Hz were **are** considered in *SIMPACK*. Hub, nacelle, drive train and foundation were **are** defined as rigid bodies. The centrifugal force induced by the blade rotation and the gravity force were **are** considered. The time-integrator *SODASRT\_2*, a **R3:S2-h** A variable step-size integrator, was **is** used to ensure that at each time step all model states were **are** kept within predefined tolerances.

### 3.4.3 Fluid-structure coupling

An explicit coupling scheme is applied between *SIMPACK* and *FLOWer* with both solvers running in a sequential way. After each physical time step, information is exchanged, with *SIMPACK* using the aerodynamic loads of the previous time step to calculate the deformations. The communication is realized by means of files containing deformations or loads at a total of 106 marker positions, of which 29 markers are allocated to each blade, 17 markers to the tower, and one marker each to the nacelle and hub. The surface mesh is reduced to a point cloud that deforms according to the markers. The cells of the volume mesh are linked to the point cloud via radial basis functions and thus also deform accordingly. Further details can be found in Klein et al. (2018) and a validation of the *FLOWer-SIMPACK* coupling with an elastic cantilever beam in Klein (2019).

## 3.5 Simulation cases

To validate the wind field simulated with *FLOWer*, the complex terrain in Perdigão was **is** simulated without turbine, as described in Sect. 3.2. This simulation is referred to as the *empty* case. The evaluation started **s** after the simulation of 300s; **which-were**. This initialisation is necessary to propagate the imposed turbulence through the domain.

**This** The *empty* case was **is** also the basis of the simulation with the turbine I82 in the complex terrain, referred to as *terrain* case. The turbine with its multiple component meshes was **is** integrated into the Perdigão terrain mesh with the **simulated** propagated turbulent terrain flow (after 300s). 16 revolutions without fluid-structure coupling were **are** simulated with a time step corresponding to  $2^\circ$  azimuth to reduce the disturbances due to the integration and to develop the turbine wake. Then two revolutions were **are** simulated with FSI to obtain the quasi steady deformation of blades and tower. A calibrated artificial damping was **is** applied to attenuate the starting oscillations due to the uninitialised structural model. For the evaluation simulation, the artificial damping was **is** switched off and the time step was **is** reduced so that it corresponds to  $1^\circ$  azimuth. The turbine was **is** simulated with a constant rotational speed of  $n = 16.87$  rpm, which corresponds to the thirty-minute average (10 May 2017 from 15:15:00 UTC) of the turbine's rotational speed at the site. The corresponding pitch angle of the generic I82 is  $\beta = 4.06^\circ$ .

**Table 2.** Definition of *FLOWer* simulation cases with their inflow conditions and computational mesh size.

Case name	Terrain	Turbine	$u(z)$	$v(z)$	$w(z)$	$u_{ref}$ [m s <sup>-1</sup> ]	$TI$ [%]	$L$ [m]	$N_{cells}$ [10 <sup>6</sup> ]
<i>empty</i>	Perdigão	-	profile	profile	profile	3.71	26.5	28.25	242.1
<i>terrain</i>	Perdigão	I82	profile	profile	profile	3.71	26.5	28.25	301.2
<i>turbulent</i> <span style="background-color: #90EE90;">flat+turb</span>	flat	I82	profile	0	0	10.16	10.2	30.51	93.3
<i>uniform</i> <span style="background-color: #90EE90;">flat+unif</span>	flat	I82	$u_{ref}$	0	0	10.09	-	-	67.3

The two reference simulations with *FLOWer* of the I82 in flat terrain used the same operating conditions and were also run as coupled simulations. One simulation, referred to as *turbulent case*, had an inflow with atmospheric turbulence and flat+turb, has a turbulent inflow with R3:S7-e vertical wind shear. It was created using the method described in Sect. 3.3. However, for this case, the *E-Wind* results were taken from a slice at the turbine position at the top of the ridge. Hence, the effects of orography and vegetation on the horizontal wind speed  $WS$ , turbulence intensity  $TI$  and length-scale  $L$  were only included in the *FLOWer* input to the extent that *E-Wind* was able to reproduce them. The occurring vertical velocity component at the turbine position was neglected in this setup. The second reference simulation, referred to as *uniform case*, had flat+unif, has an uniform inflow. The wind velocity was taken from the *E-Wind* result on hub height and was 10.09 ms<sup>-1</sup>. The flat background meshes for the reference simulations are 50 rotor radii ( $R$ ) long (12.5 $R$  upstream of the rotor plane) and 25 $R$  wide and high. For turbulent inflow with no-slip wall and BL cells and for uniform inflow with slip wall and no BL cells at the bottom.

All evaluated simulations with turbine, including the reference simulations, were run with fluid-structure coupling. A comparison with a rigid turbine was not considered, as the findings from Klein et al. already show that the blade-tower interaction, a key mechanism investigated in the following, is dominated by the blade-tower distance, which is massively reduced when the aeroelasticity of the blades is taken into account.

The four simulation cases with the respective inflow conditions are summarized in Table 2, with the longitudinal velocity  $u_{ref}$ ,  $TI$  and  $L$  as reference values at the inlet on 77 m a.g.l.. The overall number of cells  $N_{cells}$  per setup is also given.

#### 4 R2:G3-a R3:S15-a Results Part 1 – Terrain flow in Perdigão

The aim of the simulation chain is to model surface pressure fluctuations under realistic operating conditions in complex terrain in Perdigão. Therefore, the simulated terrain flow without turbine (*empty case*) was validated first, followed by the evaluation of the simulated turbine (cases *uniform*, *turbulent*, *terrain*):

The simulation of the terrain in Perdigão was intended to reproduce the measured flow situation on 10 May 2017 from 15:15:00 UTC with an inflow from southwest (230°):

R2:G3-g The validation of the flow field in the complex terrain at Perdigão simulated with *E-Wind* as well as with *FLOWer* is presented in the first part of the results. This demonstrates the suitability of the process chain for the detailed simulation of

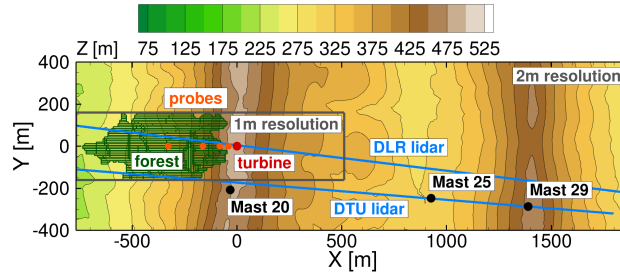


**Figure 6.** Location of lidar planes, met masts and probe positions in Perdigo relative to the turbine and properties of the *FLOWer* setup.

**Table 3.** Comparison of *E-Wind* result and *FLOWer* result (180s averaged) with met mast data (30min averaged).

		<i>E-Wind</i>					<i>FLOWer</i>				
Met	$z$	$\Delta WS$	$\Delta w$	$\Delta WD$	$\Delta TI$	$\Delta WS$	$\Delta w$	$\Delta WD$	$\Delta TI$		
mast	[m a.g.l.]	[ $\text{ms}^{-1}$ ]	[ $\text{ms}^{-1}$ ]	[ $^{\circ}$ ]	[% <b>R3:S11-a</b> pp.]	[ $\text{ms}^{-1}$ ]	[ $\text{ms}^{-1}$ ]	[ $^{\circ}$ ]	[% <b>R3:S11-b</b> pp.]		
20	20	0.2	-0.4	1.4	1.1	0.3	-0.4	5.0	-9.3		
	60	0.1	-0.4	1.1	0.7	-0.2	-0.1	6.8	-7.7		
	100	0.0	-0.8	0.4	2.2	0.2	-0.7	3.7	-4.7		
25	20	-2.0	0.2	50.1	51.2	-1.7	0.3	77.2	35.2		
	60	-1.6	0.3	55.8	27.7	-2.2	0.6	57.1	17.7		
	100	-0.2	-0.1	40.7	-3.1	-1.6	0.2	31.5	-4.5		
29	20	-0.7	-0.1	5.0	-6.9	0.0	0.1	-1.6	-15.0		
	60	-0.6	0.2	8.2	-6.7	-1.1	-0.4	8.2	-11.5		
	100	-0.2	0.3	2.3	-9.2	-1.8	0.0	8.6	-5.0		

$\Delta = \text{Simulation} - \text{Measurement}$ .

**R3:S11-c** pp.: percentage points

the complex terrain. Two lidar planes (Menke et al., 2019a; UCAR/NCAR, 2019a) and the met masts (UCAR/NCAR, 2019b) shown in Fig. 6 were are used for validation (30min average).

#### 4.1 Validation of precursor simulation

At mast 20, which was is used for calibration, a very good agreement between simulation and measurements for  $WS$ ,  $WD$  and  $TI$  could be is achieved (see Table 3). Figure 7 shows the difference of the horizontal component of the line-of-sight velocity wind velocity  $u_h$  in the DTU lidar plane between the *E-Wind* result and the lidar measurement. The  $x$ -axis describes the distance  $D$  from mast 20 in the lidar plane. Only minor differences are observed in front of the first ridge, which justifies the extraction of the data for the generation of the inflow for the *FLOWer* simulation from the precursor simulation at the base of the first ridge.

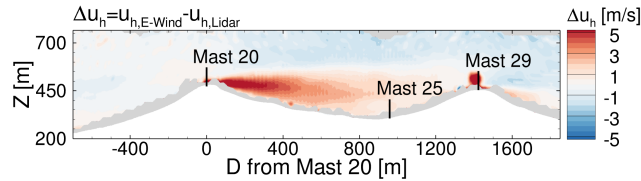


**Figure 7.** Comparison of the horizontal **component of the line-of-sight velocity** **wind-velocity**  $u_h$  in the DTU lidar plane between the *E-Wind* result and the measurement.

The recirculation zone behind the first ridge is **strongly** underpredicted in *E-Wind*. The main reason is probably the smoothing of the terrain due to the mesh resolution of 10m. Satellite images of the site show rocky terrain at the top of the ridge that could trigger early flow separation. Since these terrain features are not resolved in *E-Wind*, the flow stays attached to the ground longer and separates later, resulting in a smaller recirculation region. **Moreover, it is well known that RANS models have difficulties in accurately predicting the size of and the flow within a recirculation zone. Consequently, large differences between simulation and measurements are observed in the valley at mast 25, especially at the lower heights. In the valley, large differences between simulation and measurements could be observed, especially for the lower heights. For mast 25,  $WS$  is underestimated,  $WD$  is off by about  $50^\circ$  and  $TI$  is overestimated in the simulations. It is well known that RANS models have difficulties in accurately predicting the size of and the flow within a recirculation zone.** Furthermore, there may be some microscale or other physical effects that are not modelled in *E-Wind* (e.g. anabatic winds). **For** **At** mast 29 **at on** the second ridge, a **good better** agreement with the measurements **was** **can again be** observed.

#### 4.2 Validation of **unsteady terrain simulation**~~simulated unsteady flow field~~

The **unsteady** results of the detailed DDES with *FLOWer* of the wind field in Perdigão without turbine (case *empty*) **were** **are** averaged for 180s (equivalent to three times the duration of the Mann turbulence box) and compared with measured data. Figure 8 shows the simulated mean horizontal **component of the line-of-sight velocity** **wind-velocity** in the DTU lidar plane  $u_h$  of the *empty* case and the difference to the measurement. The speed-up at the first ridge agrees very well with the measurement, which is important to simulate the **inflow to local flow at** the turbine **position** correctly. The velocity in the recirculation zone **was** **is** captured much better than in the steady-state precursor simulation with *E-Wind*, but still the differences in the valley between the ridges are the largest.

A comparison with the met mast data in Table 3 confirms this. At mast 20, both the horizontal wind speed  $WS$  and the wind direction  $WD$  fit very well over the entire mast height, indicating that the **R3:S7-f** **vertical wind** shear **was also is** met. The vertical velocity  $w$  and thus the flow inclination is slightly underpredicted. The simulated **turbulence intensity**  $TI$  is too low **This is probably** because mast 20 ( $y = -207$  m) is not located in the finest mesh region (see Fig. 6). Therefore, the flow at this position has undergone stronger numerical dissipation than the direct inflow to the turbine. In fact, **in the region with 1 m resolution 2R in front of the turbine 77 m a.g.l., the simulated turbulence intensity the simulated TI 2R in front of the turbine 77 m a.g.l. ( $y = 0$  m), in the region with 1 m resolution,** is about 4% **R3:S11-d** **percentage points** higher than at the same

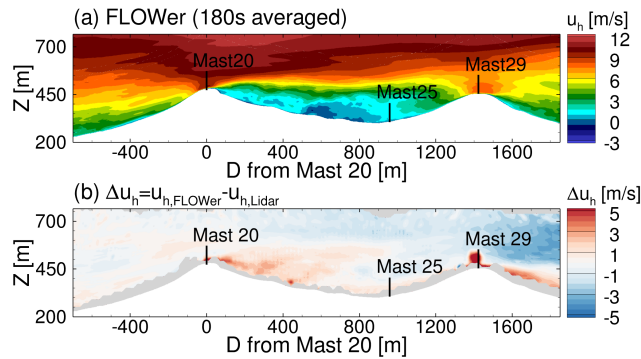


**Figure 8.** Horizontal component of the line-of-sight velocity wind-velocity  $u_h$  in DTU lidar plane, simulated with *FLOWer* (a) and comparison difference to measurement (b).

height at mast 20 in the simulation. Taking this offset into account, the simulated *TI* agrees much better with the measured value on the first ridge. The slightly larger deviation at lower heights could might be due to the lack of forest wake in the simulation at mast 20. Mast 25 in the valley shows large differences especially in the wind direction. This is probably due to a thermally driven valley flow (Fernando et al., 2019), whose physical source was is included neither in the *FLOWer* simulation nor in *E-Wind*. This missing flow also causes the wind speed to be too low and thus the *TI* to be too high. On the second ridge at mast 29, the agreement between simulation and measurement is better again. The too low mean-velocity *WS*, which can also be seen in Fig. 8, could might be due to a still too small a distance of the second ridge to the outlet BC in the simulation, where not fully dissipated vortices can cause a backward inflow. The lack of vegetation behind the first hill together with the increasing numerical dissipation with propagation distance in the simulation resulted, as expected, in much too low simulated *TI* values.

The energetic energy containing vortices in the simulation of the flow over the terrain in Perdigão were are identified by calculating the power spectral density (PSD) using Welch's method with Hann window (amplitude corrected), 66% overlap and three segments. The horizontal velocities at four positions 77 m a.g.l. in the direct inflow of the turbine position (see probes in Fig. 6) were are evaluated. Figure 9 shows the spectra compared to the measurement at mast 20 at a height of 80 m a.g.l., where the energy cascade is proportional to  $f^{-5/3}$  as given by Kolmogorov for the inertial subrange. The simulation resolves this energy cascade for more than an order of magnitude before numerical dissipation causes a drop for frequencies  $f > 1$  Hz. The accurately-resolved part of the spectrum covers the relevant load range for wind turbines, since the blade passing frequency (BPF) for the turbine integrated into the terrain later in the simulation corresponds to  $f_{BPF} = 0.84$  Hz. Further up the ridge, turbulence with higher frequencies is resolved as the flow accelerates, which agrees with Spalart (2001) who found that the smallest eddies resolvable with DES occur with a frequency of  $f_{max} \approx u \cdot (5 \cdot \Delta_0)^{-1}$ .

It can be concluded that the DDES of the complex terrain in Perdigão with *FLOWer* using the inflow generated from *E-Wind* results provides an accurate site- and situation-specific mean flow field as well as resolved turbulence up to  $f \approx 1$  Hz for the evaluated situation. R3:S12-a gives a realistic flow field on the first ridge. There, both the mean flow field and the resolved

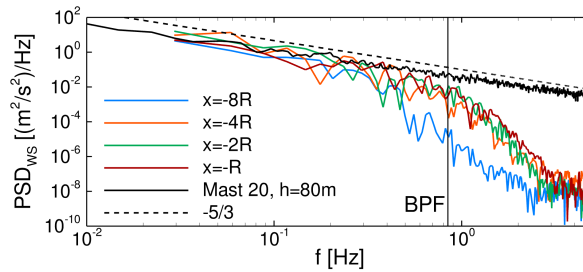


**Figure 9.** Development of power spectral density of horizontal wind speed  $W_S$  upwind of the turbine in 77 m a.g.l. in *FLOWer*.

turbulence up to  $f \approx 1$  Hz agree with lidar and met mast data. This ensures that the following studies on the influence of the inflow on the turbine aerodynamics are also applicable to reality. Further downstream, however, in the valley as well as on the second ridge, the simulated flow field deviates from the measured situation due to missing physical phenomena and numerical dissipation.

## 5 R2:G3-b R3:S15-b Results Part 2 – Impact of inflow on turbine aerodynamics Turbine in complex terrain

R2:G3-h The overall goal of the presented simulation chain is to model surface pressure fluctuations on a wind turbine under realistic operating conditions in complex terrain. In the second part of the results, the fluid-structure coupled simulation of the I82 turbine in the complex terrain The results of the *FLOWer* simulation with the fluid-structure coupled I82 turbine at Perdigoão (case *terrain*) were is evaluated for 16 revolutions after initialising initialisation of the wake and the deformations as described in Sect. 3.5.

The flow field around the turbine, its global loads and deflections as well as surface pressure fluctuations on blades and tower were are investigated. The results were are compared with the reference simulations in flat terrain (cases *uniform flat+unif* and *turbulent flat+turb*) when appropriate.

### 5.1 R3:S16-a Turbine wake in complex terrain Impact on global terrain flow

The DLR lidar was is in-plane with the turbine and orientated almost parallel to the mean-flow  $WD_{hub}$  of this situation (see Fig. 6) and is therefore well suited to evaluate the impact of the turbine on the terrain flow field. Figure 10a shows the difference between the *FLOWer* simulation with resolved turbine (case *terrain*) and the simulation without turbine (case *empty*). The mean horizontal wind speed  $u_h$  in the DLR lidar plane was is averaged over 16 revolutions and the corresponding 60s from the *empty* simulation, respectively. The upwind induction zone in front of the turbine is relatively weak small, while the wake is quite distinct up to  $\approx 340$ m behind the turbine. The wake does not follow the terrain but drifts slightly upwards. This fits well with the findings of Wildmann et al. (2018) from measurements under neutral stratification, however the velocity deficit decays faster in their study. A comparison with the measured mean horizontal velocity  $u_h$  for the selected situation (see Fig. 10b) also shows a faster decay. It should be noted, however, that the DLR lidar plane has an offset of  $\approx 7^\circ$  from the mean

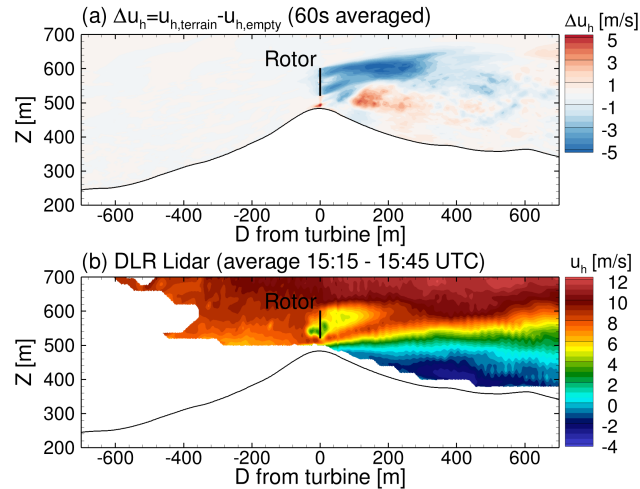


**Figure 10.** Difference of horizontal component of the line-of-sight velocity wind-speed  $u_h$  in the DLR lidar plane between the *FLOWer* results of (a) the simulation with and without turbine and (b) the measured  $u_h$ .

460 wind direction, which leads to a drift of the wake out of the measured plane. In the simulation, the flow is unintentionally more aligned with the DLR lidar plane, which is evident from the offset  $\Delta WD$  found for mast 20 in Table 3. Moreover, the too low *TI* in the simulation causes the wake to be slightly too stable. Overall, the influence of the turbine on the terrain flow is well captured.

## 5.2 Global Loads and deflections

465 Figure 11 shows the blade tip displacement out of the rotor plane  $\Delta x_{oop}$  of one blade for all cases. The *turbulent* flat+unif case shows a clear sinusoidal trend mainly caused by the gravity load and the rotor tilt. The blade deformation overcompensates the pre-bend, so gravity contributes more to the out-of-plane displacement when the blade is pointing upwards. The impact of the blade-tower interaction, ~~and hence the unsteady aerodynamic loads,~~ on the blade deformations is only weakly recognisable by the faster decrease of  $\Delta x_{oop}$  shortly after the tower passage. The inclusion of turbulence in the reference simulation flat+turb

470 massively increases the amplitude of fluctuations that occur once per revolution. This is due to the large variations in wind speed over the rotor disk arising from R3:S7-g vertical wind shear and turbulence. ~~In both cases, turbulence predominates over shear effects, which can be seen in~~ R3:S7-h However, the effects of turbulence outweigh those of vertical wind shear, as can be seen from the irregular pattern. The turbulent eddies are smaller than the rotor disk ( $L < 2R$ ) and therefore cause load oscillations with the rotation frequency. Moreover, the rotational periodicity is superimposed by stochastic broadband fluctuations caused

475 by very small eddies. ~~The out-of-plane deformations mostly follow the aerodynamic blade bending moment  $M_y$ .~~ However, a A comparison between the *turbulent* flat+turb and the *terrain* case shows that the inflow turbulence cannot be generalised and has a very unique impact on the ~~behaviour of the turbine~~ R3:S17-a loads and deformations of the blades in each case. This illustrates how important it is to model the inflow realistically and site specific.

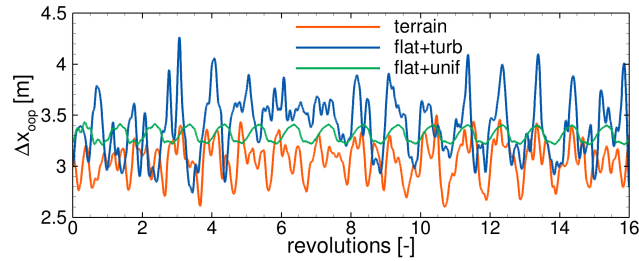


**Figure 11.** Deformation of blade tip out of the rotor plane  $\Delta x_{opp}$  for all cases.

**Table 4.** Local inflow to the turbine and global loads on the turbine for all simulation cases ~~with turbine~~.

Case name	$U_{ref}$ [m s <sup>-1</sup> ]	$\gamma$ [°]	$\overline{\Delta x_{opp}}$ [m]	$\overline{P}$ [MW]	$\overline{F}_x$ [kN]
<del>turbulent</del> flat+unif	9.2	0.2	3.31	1.5	221
<del>turbulent</del> flat+turb	9.5	-1.6	3.33	1.6	230
terrain	8.9	13.6	3.06	1.2	196

The ~~small~~ difference  $\delta$  in the mean blade tip deformation  $\overline{\Delta x_{opp}}$ , given in Table 4, ~~is~~ ~~are~~ due to differences in the global loads caused by slightly different flow conditions at the turbine position ~~in the three simulations~~. Table 4 also lists ~~T~~ the local inflow to the turbine ~~is characterised~~ characterized by a mean velocity  $U_{ref}$  and a mean flow inclination angle  $\gamma$  one  $R$  in front of the turbine at hub height. ~~Table 4 summarizes the flow at the turbine position for the three cases and lists the different~~ as well as ~~the~~ extracted mean powers  $\overline{P}$  and mean acting thrusts  $\overline{F}_x$ . ~~The inflow generation described in Sect. 3.5 was intended to result in similar loads at the turbine.~~ The intention has been to obtain similar flow conditions at the turbine position and thus similar loads in the three simulations (compare Sect. 3.5). However, it turned out that the underlying *E-Wind* results overestimated the velocities at the turbine position. ~~Due to a recirculation zone that was too small, the streamlines in E-Wind followed the terrain too closely and were thus more curved, which led to too high an acceleration.~~ **R3:G2-a** Due to the too small recirculation zone in E-wind, the streamlines follow the terrain more closely than in FLOWer and are therefore more curved, resulting in greater acceleration. The unsteady aerodynamic effects analysed in the following are not significantly altered by differences in mean loads and can still be compared between the cases.

### 5.3 Surface pressure on tower

The surface pressure  $p$  and its distribution are the dominant source of the aerodynamic loads and are evaluated on the tower in the following. In many respects, be it fatigue loads or acoustic emissions, the fluctuations and the distribution of the acting forces are of greater importance than the magnitude of the steady load. Figure 12 shows contour plots of the standard deviation  $\sigma$  of the surface pressure on the tower for all cases. In the plots the angle  $\Phi$  on the  $x$ -axis corresponds to the circumferential

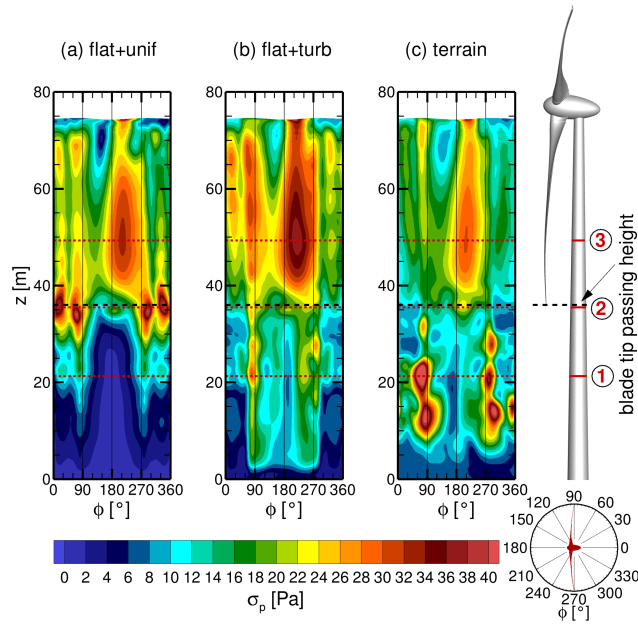


**Figure 12.** Standard deviation  $\sigma$  of surface pressure  $p$  on tower for all cases (a)-(c).

position of the tower, where  $180^\circ$  is the upwind side where the blades pass. Three main areas of interest can be distinguished, marked with horizontal dotted lines in red (①, ②, ③). Below the blade tip passage (①), inflow turbulence increases the fluctuations, especially in the *terrain* case, while at the height of the blade tip passage (②), the fluctuations are actually reduced in both cases with turbulent inflow compared to uniform inflow. The main effect of the blade on the tower is at around 505 50 m height (③) on the side of the descending blade ( $\Phi \approx 210^\circ$ ) for all cases. The cause of these observations is examined separately for each height in the following.

### 5.3.1 R2:G3-c R3:S15-c Surface pressure on tower at height ①

Below the blade passage on height ①, the time series of the surface pressure fluctuations  $p - p_{avg}$ , where  $p_{avg}$  is the local time average, on a line around the tower were are extracted and plotted as contour plots in Fig. 13. The uniform inflow causes 505 distinct, periodic patterns, especially on the back and crosswind sides of the tower ( $120^\circ > \Phi > 240^\circ$ ), which increase in intensity over time. The two cases with turbulent inflow, on the other hand, are dominated by larger patterns that are less regular. Nevertheless, the turbulent flat+turb case develops a fine pattern on the tower back after some time. For the *terrain* case, patterns are by far the largest. Opposing pressure fluctuations occur at the tower sides, which remain stable for multiple revolutions and then swap.

510 With a transformation to the frequency domain using Welsh's method (compare Sect. 4.2), the observed pattern can be better characterised. The PSDs in Fig. 14 show that for uniform inflow, the main fluctuations occur at the tower sides and back at discrete frequencies that are not multiples of the BPF. These pressure fluctuations can be associated with a periodic separation

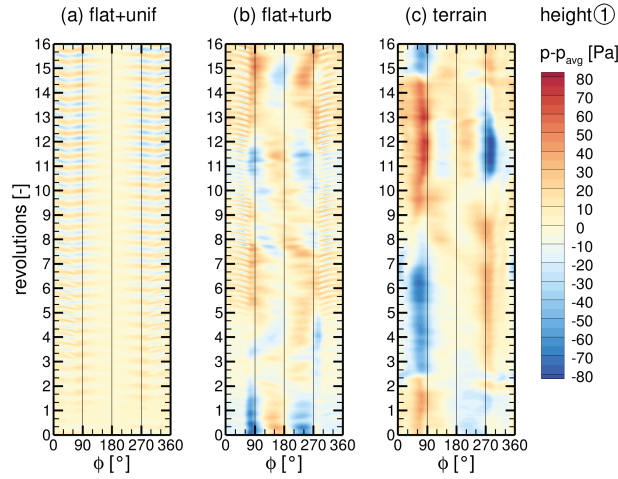


**Figure 13.** Time series of surface pressure fluctuations  $p - p_{avg}$  on a line around the tower on height ① for all cases (a)-(c).

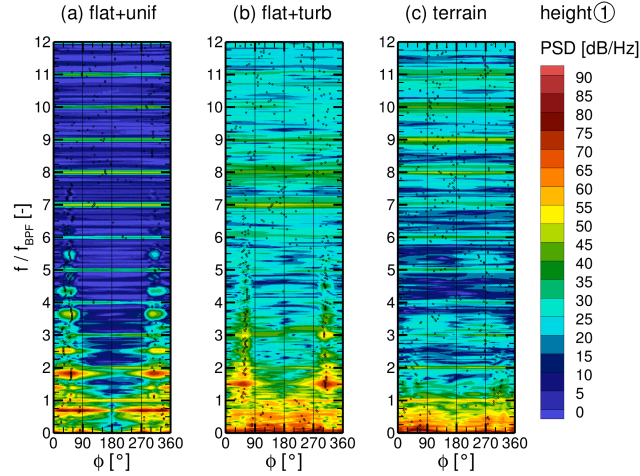


**Figure 14.** Power spectral density of surface pressure fluctuations on a line around the tower on height ① for all cases (a)-(c).

known as the Kármán vortex street. However, according to Horvath et al. (1986), the local Reynolds number of the tower  $Re \approx 2.5 \cdot 10^6$  falls into the supercritical regime, where vortex shedding can occur over a wide range of frequencies and is quite unstable or even not observed at all in some experiments. Nevertheless, they found two dominant shedding frequencies in their experiments for supercritical  $Re$ -numbers. This fits well with the observation in Fig. 14a with two dominant frequencies at  $f = 0.59\text{Hz}$  and  $f = 1.55\text{Hz}$ . Considering the time history in Fig.13, it can even be stated that the shedding characteristic changes over time, which underlines the instability of the vortex street.

Figure 15 shows the instantaneous vortex structures visualized with the  $\lambda_2$ -criterion, coloured with the vertical component of vorticity  $\omega_z$ . With uniform inflow, coherent vortex cells with constant shedding frequency form and extend over the entire

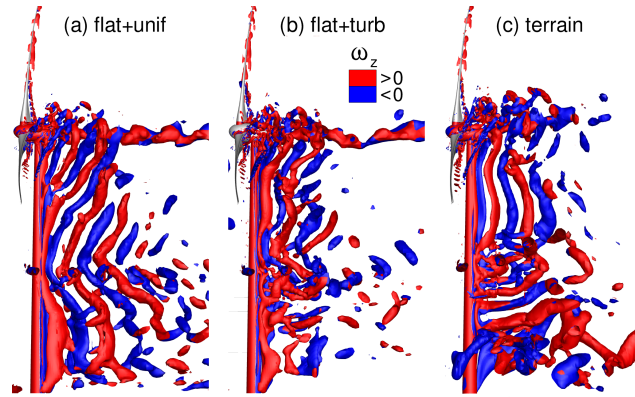


**Figure 15.** Vortex structures after 16 revolutions visualized with  $\lambda_2$ -criterion and coloured with vertical vorticity  $\omega_z$  for all cases (a)-(c).

tower height. This phenomena is well known for tapered cylinders (e.g. Johansson et al. (2015)), although it is remarkable that only one vortex cell forms over the entire tower height, not even broken up by the blade tip vortices (not shown). Therefore, using the local tower diameter to calculate the Strouhal number of the shedding frequencies is not appropriate. Using the mean tower diameter gives  $St = fd/u = 0.18$ , which fits the experimental results of Jones Jr. (1968), and  $St = 0.48$ , which is similar to the higher eddy-shedding frequency measured by Horvath et al. (1986) and simulated by Rodríguez et al. (2015).

Turbulence in the inflow hampers the periodic vortex shedding on height ①, as shown by the reduction of discrete frequencies in the PSD for the *turbulent flat+turb* case and an absence of discrete frequencies in the *terrain* case in Fig. 14. The vortex structures in Fig. 15b and 15c in the lower tower section confirm this. Especially in the *terrain* case, rather horizontal, stream-wise vortex structures tend to occur at the tower and the coherence in the vortex shedding is suppressed in lower tower regions. This vortex shape is triggered by the terrain flow in two different ways. First, the *sheared*-acceleration of the mean flow  $\Delta u$  due to the slope of the ridge rotates and stretches the *vertical vorticity  $\omega_z$  into streamwise vortices with increased  $\omega_x$ , as can be seen in Fig. 16.* **R3:S14-a** *turbulent structures into rather streamwise vortices. The vertical vorticity  $\omega_z$  is transferred into  $\omega_x$  in the near-ground region, as can be seen in Fig. 16. The position of the turbulence injection at  $x = -768\text{ m} + L = -740\text{ m}$  and the already increased anisotropy there at higher altitudes caused by the higher inlet velocity due to the vertical wind shear is also visible.* Belcher and Hunt (1998) found that  $\omega_x \sim \Delta u$  for turbulent flow over the top of a hill. Second, the ridge near the separation point in front of the turbine is not smooth in the crosswind direction, but has bumps similar in shape to the wedges used for passive flow control in aviation or automotive. Such obstacles give rise to strong streamwise vortex structures (McCullough et al., 1951) that interact with the flow around the lower tower in the *terrain* case. The streamwise vortices are very stable and the side changes observed in Fig. 13c are presumably triggered by corresponding temporary changes in the wind direction in the direct inflow. More general, Batham (1973) also found that turbulence suppresses coherent vortex shedding and Bruun and Davies (1975) reported a reduction in vortex shedding correlation length for turbulent flow, both for critical Reynolds numbers. For both cases with turbulent inflow, the energetic inflow turbulence (compare Fig. 9 for *terrain* case) dominates at frequencies far below the BPF at height ①, as visible in Fig. 14b and c. For all cases, the BPF and its higher

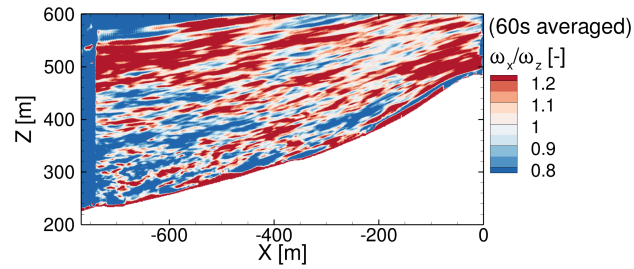


**Figure 16.** Ratio of horizontal and vertical vorticity  $\omega_x/\omega_z$  in a slice ( $y = 0$ ) upstream of the turbine.

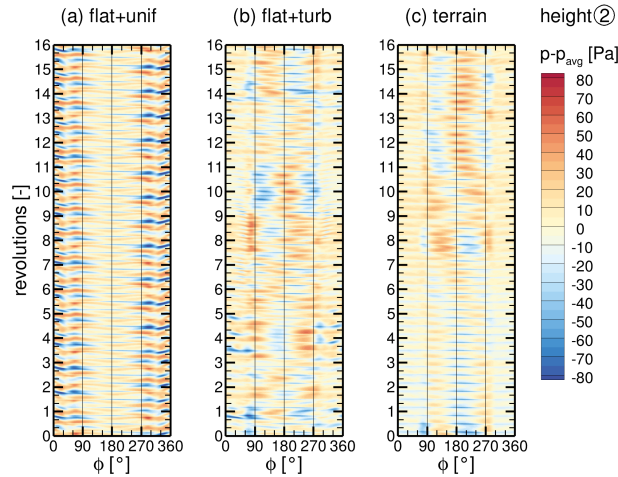


**Figure 17.** Time series of surface pressure fluctuations  $p - p_{avg}$  on a line around the tower on height ② for all cases (a)-(c).

harmonics are faintly visible in the PSDs even at this height. This shows that the consideration of realistic inflow conditions  
 545 alters the occurring physical phenomena considerably. Generically simplified setups carry the risk of enhancing stable patterns,  
 which can lead to overestimated tonalities in acoustic evaluations, for example.

### 5.3.2 R2:G3-d R3:S15-d Surface pressure on tower at height ②

The evaluation of the pressure fluctuations at height ②, where the blade tips pass, results in the pressure curves over time in  
 Fig. 17 and the PSDs in Fig. 18. With uniform inflow, the pattern of pressure fluctuations in Fig. 17 is very constant over time.  
 550 The fluctuations at the back of the tower are much stronger than at height ①, while at the tower front ( $\Phi \approx 180^\circ$ ) additional,  
 very sharp periodic fluctuations occur. The inflow turbulence in the *turbulent flat+turb* and *terrain* case clearly changes the  
 pattern also at this height. Compared to the lower height ①, a finer periodic pattern is noticeable, which occurs especially at  
 the tower front.

Almost all around the tower, but particularly at the tower front, pressure fluctuations with the BPF and its harmonics are  
 555 clearly visible for all cases at height ② in Fig. 18. They are imposed by the blade tip vortices periodically hitting the tower with

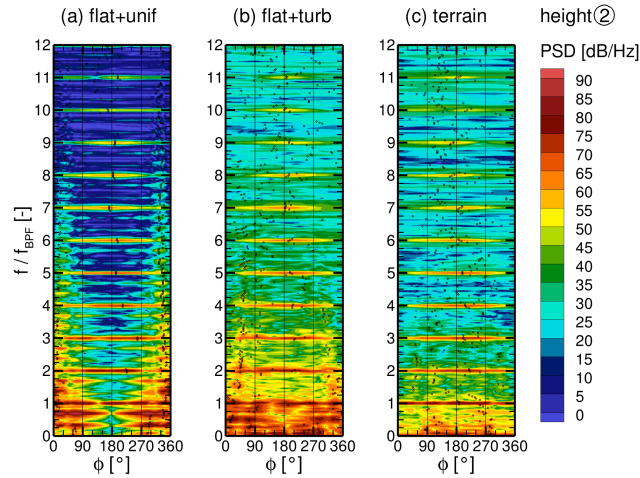


**Figure 18.** Power spectral density of surface pressure fluctuations on a line around the tower on height ② for all cases (a)-(c).

the BPF and sweeping over its circumference. Since this periodic interaction is very brief it acts as an impulse on the tower and many higher harmonics are visible in the PSD. Looking at Fig. 18a for uniform inflow, it can be seen that the strongest fluctuations still occur with a frequency  $f = 0.59$  Hz at the tower sides and back. The amplitude of these pressure fluctuations is even higher than at height ①, since the vertically stretched shed vortices have their highest vorticity in the middle part, where the local tower diameter corresponds to the mean tower diameter. For the *turbulent flat+turb* case, strong pressure fluctuations still occur at the tower sides/back below BPF associated with vortex shedding, but no discrete shedding frequency can be identified in Fig. 18b. Instead, the inflow turbulence imposes strong broadband pressure fluctuations around the whole tower for frequencies below BPF. The PSD of the *terrain* case in Fig. 18c looks remarkably different below BPF. This is because the terrain flow causes quite different vortex structures at height ②, which is evident when comparing Fig. 15b and 15c. As described, the inflow turbulence in the terrain flow is much more anisotropic, with  $\omega_z$  being converted to  $\omega_x$ , and streamwise vortices cause less pressure fluctuations on the tower surface. Moreover, the turbulence intensity  $TI$  in the near-field of the turbine is not identical between the *turbulent flat+turb* and the *terrain* case in this study, with  $TI$  being 1.5% **R3:S11-e** percentage points lower in the *terrain* case. These two factors explain the lower broadband fluctuations in the *terrain* case.

### 5.3.3 **R2:G3-e** **R3:S15-e** Surface pressure on tower at height ③

At height ③ the blade passage causes very sharp periodic pattern on the side of the descending blade ( $\Phi \approx 210^\circ$ ) for uniform inflow, as visible in Fig. 19a. The turbulent cases also show this periodic pattern (see Fig. 19b and 19c), but less sharp and superimposed by low-frequency patterns. A less strong periodic pattern on the back of the tower is also visible for all cases, indicating vortex shedding with discrete frequencies again.

Pressure fluctuations with discrete frequencies of the BPF and its harmonics have the highest amplitudes in all cases at height ③, shown in Fig. 20. The fluctuations with the BPF dominate around the whole tower since the reduced pressure on

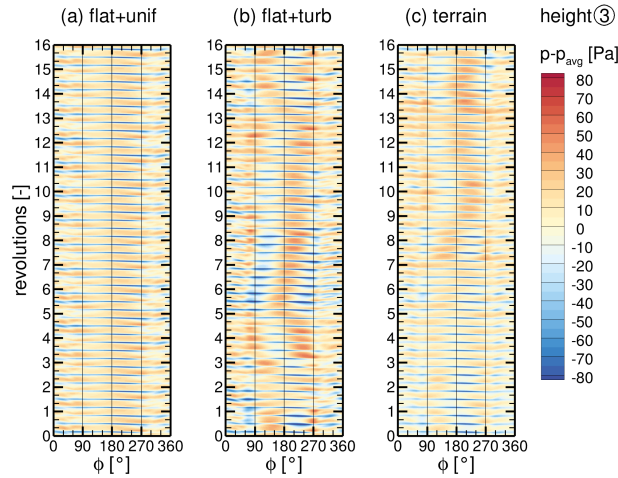


**Figure 19.** Time series of surface pressure fluctuations  $p - p_{avg}$  on a line around the tower on height ③ for all cases (a)-(c).

the suction side of the blade extends around the whole tower when the blade passes. The strongest fluctuation with BPF occur on the side of the descending blade ( $\Phi \approx 210^\circ$ ), marked with black symbols in Fig. 20. This was also found by Klein (2019) and is due to a speed up of the flow between tower and the approaching blade, known as Venturi effect, locally enhancing the pressure reduction. For the higher harmonic pressure fluctuations of the BPF the maxima slightly drift towards the tower front as the frequencies increase. With uniform inflow, even at height ③ where the blades pass, the same vortex shedding frequency is pronounced at the tower sides and back as at the lower heights, as visible in the PSD in Fig. 20a. This confirms that coherent vortex cells stretch over the entire tower height for uniform inflow, even with the blade wake interaction and a tapered shape of the cylinder. The curved shape of the vortex cells in Fig. 15a is due to the reduced flow velocity behind the blades caused by the blade induction, resulting in a slower downwind propagation of the vortices. The *turbulent flat+turb* case shows the same vortex shedding frequency, but much less pronounced, with a more broadband character of the pressure fluctuations below BPF. At height ③, the *terrain* case shows vortex shedding for the first time with a fairly discrete frequency at the tower back, however, at  $f = \text{BPF}/2$ . Figure 15c shows the coherent vortices at the upper tower. As mentioned, the horizontal inflow vortices prevent the formation of strong vortex cells extending over the entire tower height and thus the blade passage impulse is dominant enough to induce a periodic vortex shedding on the upper tower, one vortex per blade passage with opposite circulation. This interaction between blade passage and vortex shedding *was is* also described by Gómez et al. (2009), who performed two-dimensional simulations of the blade-tower interaction.

Figure 21 shows the maximum amplitude of the pressure fluctuations on the tower with the BPF ( $f_{BPF} = 0.84 \text{ Hz}$ ) and its first two higher harmonics (1.69 Hz and 2.53 Hz) and the circumferential position  $\Phi$  where they occur. Behind the blade passage, above  $z = 35 \text{ m}$ , neither the position nor the amplitude of the strongest pressure fluctuations with BPF or the first two higher harmonics are significantly altered by the different inflow conditions. This means that the mechanisms of the blade-tower interaction remain unchanged.

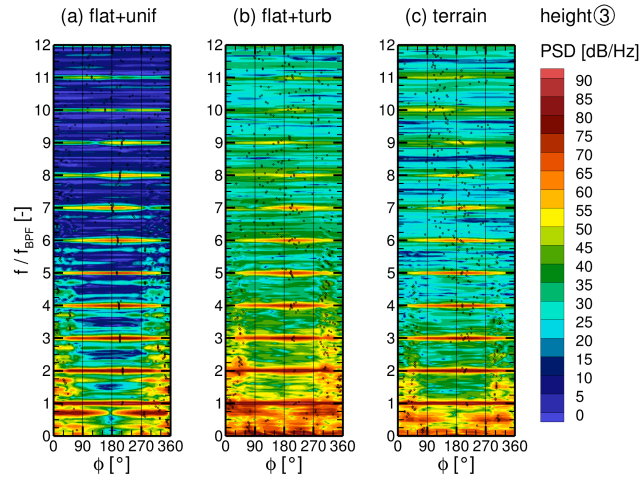


**Figure 20.** Power spectral density of surface pressure fluctuations on a line around the tower on height ③ for all cases (a)-(c).

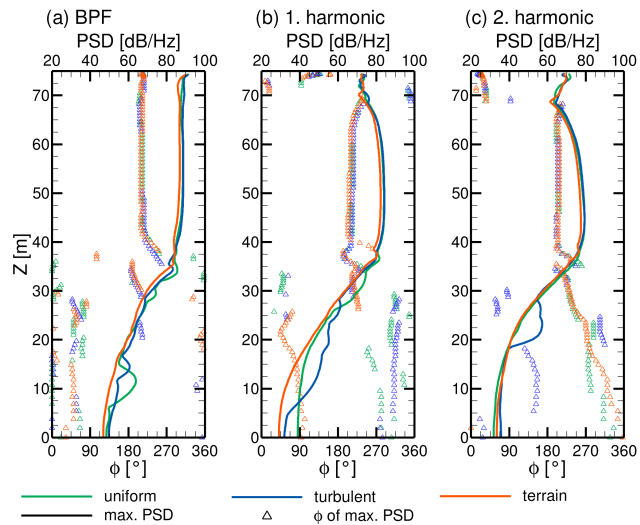


**Figure 21.** Maximum amplitude of the PSD of the surface pressure fluctuations per height and their circumferential position on the tower for BPF (a), first (b) and second (c) higher harmonic.

The observations ~~made lead to the conclusion~~ show that the surface pressure fluctuations on the tower are dominated by a superposition of blade-passing effects and tower vortex shedding, as also described by Klein et al. (2018). The inflow turbulence itself characteristic has no significant influence on the fluctuations at the tower, ~~however, it is shown how crucial it is to take it into account realistically nevertheless, since it massively alters the vortex shedding characteristic and thus the periodicity of the surface pressure fluctuations which can drive the emergence of acoustic low-frequency tonalities.~~ **R3:G1-d** in connection with the blade-tower interaction. However, pressure fluctuations due to vortex shedding from the tower are strongly inflow-de-

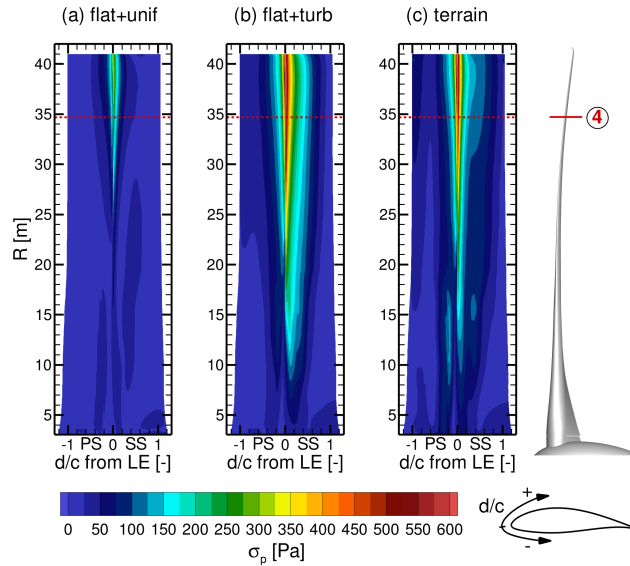


**Figure 22.** Standard deviation  $\sigma$  of surface pressure  $p$  on one blade for all cases (a)-(c).

pendent. It is therefore crucial to take the inflow into account realistically in order to correctly capture the periodicity of the surface pressure fluctuations, which can, for example, drive the occurrence of acoustic low-frequency tonalities.

#### 605 5.4 Surface pressure on blades

Besides the tower, the blades are the turbine components with the largest surface area, ~~which makes them relevant low-frequency emitters~~. Moreover, they ~~are the components with highest~~ generate most of the aerodynamic loads. Figure 22 shows contour plots of the standard deviation  $\sigma$  of the surface pressure on one blade for all cases. In the plots the blade is unwound and the arc length  $d$  from the leading edge (LE) is normalized with the local chord length  $c$ , where positive values belong to the suction side (SS) and negative values to the pressure side (PS) respectively. Pressure fluctuations are the strongest close to the LE for outer blade radii. Inflow turbulence significantly increases the fluctuations and broadens the region in both ~~turbulent flat+turb~~ and the *terrain* case. To further look into details a position ④ at 85% blade radius marked with the red line ~~was~~ is chosen. At this radial position the blade generates the highest thrust per meter.

The time series of the pressure fluctuations  $p - p_{avg}$  at the blade radius ④ in Fig. 23 show a periodic pattern over the whole circumference with a frequency of once per revolution for the ~~turbulent flat+unif~~ case. Towards the LE, the fluctuations are by far the strongest and opposite compared to the main part of the airfoil. The reversal of the pressure pattern between descending (from full to half revolution) and ascending (from half to full revolution) blade is due to the rotor tilt. It causes the effective angle of attack  $\alpha$  at radius ④ to be slightly less for the descending blade than for the ascending ( $\Delta\alpha \approx 0.28^\circ$ ). This leads to a small periodic shift of the stagnation point, increasing the pressure on the SS close to LE for the descending blade. In contrast, the effective inflow velocity  $u_{eff}$  at the blade at radius ④ is slightly higher for the descending blade than for the ascending

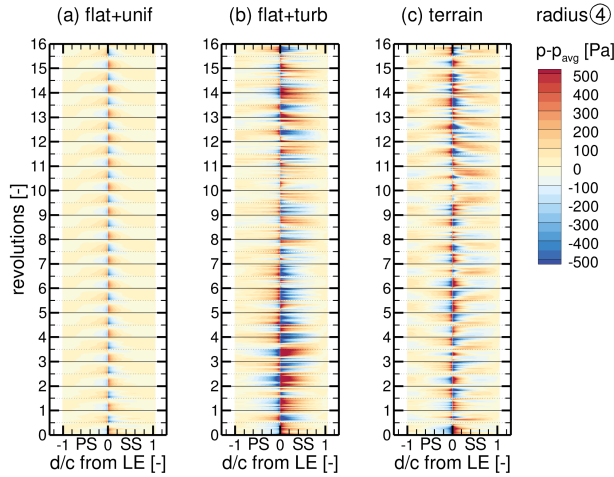


**Figure 23.** Time series of surface pressure fluctuations  $p - p_{avg}$  along a blade section at radius ④ for all cases (a)-(c).

( $\Delta u_{eff} \approx 1.7 \text{ ms}^{-1}$ ). This dominates the global blade load and leads to a lower pressure on the SS and higher one on the PS from  $\approx 0.4c$  to the trailing edge for the descending blade. These effects also occur for the *turbulent flat+turb* and the *terrain* cases, but are superimposed by the unsteady changes in local flow velocity and direction caused by the inflow turbulence, which generates additional stochastic pressure fluctuations. The *coupled* unsteady blade deflection (see Fig. 11) additionally changes  $u_{eff}$  and  $\alpha$ , resulting in a complex interaction. As on the tower, the *terrain* flow causes less strong fluctuations compared to the *turbulent flat+turb* case due to the described difference in the inflow turbulence. In addition, the inclined flow reduces  $\alpha$  for the ascending blade and decreases it for the descending blade, respectively. This counteracts the periodic angle of attack variation and consequently load fluctuations caused by the tilt. Furthermore, the slightly **R3:S7-i** vertically sheared inflow ( $\Delta u \approx 0.5 \text{ ms}^{-1}$  over the rotor) in these two cases marginally increases the blade loads in the upper half of the revolution, reducing the pressure on SS and increasing it on PS. For all cases, the tower passage causes a very sharp, impulsive disruption of the pressure pattern (see Fig. 23 at each half revolution) by a sudden reduction in  $\alpha$  due to the reduced flow velocity in front of the tower and due to the acceleration of the flow between blade and tower, known as the Venturi effect. In addition, the higher pressure in the tower dam region is imposed on the blade.

A transformation into the frequency domain, depicted in Fig. 24, confirms the observations. For the *turbulent flat+unif* case at the blade radius ④, peaks are visible at the rotational frequency  $f_t = 0.28 \text{ Hz}$  and its multiples. The peak at  $f_t$  is caused by a combination of the tilt effect and the blade-tower interaction. The tilt effect is sinusoidal and therefore the higher harmonics are caused solely by the impulsive blade-tower interaction. The PSD also shows that the pressure fluctuations are not limited to the LE but occur around the whole blade, which is difficult to see in Fig. 23a. Inflow turbulence in the *turbulent flat+turb* and the *terrain* case dominates at the blade radius ④ above  $f_t$  and masks the higher harmonics caused by the blade-tower interaction, resulting in a broadband characteristic of the pressure fluctuations. The most pronounced pressure fluctuations occur in all inflow cases at the rotational frequency. However, the maximum amplitude for that frequency is slightly stronger

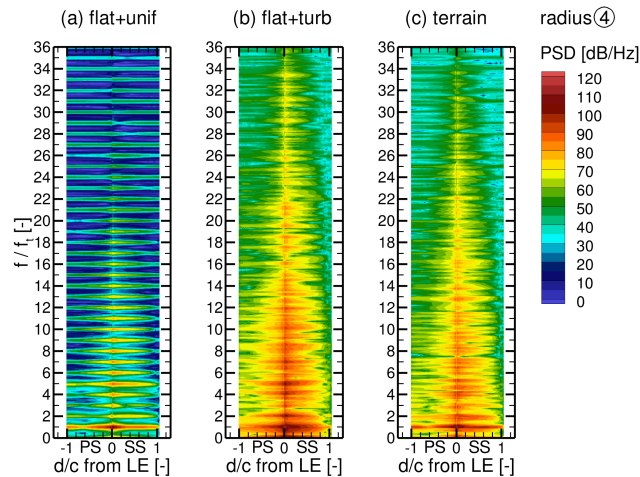


**Figure 24.** Power spectral density of surface pressure fluctuations on a line around the blade at radius ④ for all cases (a)-(c).

in the *turbulent* **flat+turb** case than for uniform inflow due to the **R3:S7-j** **vertical wind** shear effect, which is also sinusoidal, and is further amplified in the *terrain* case by the inclination effect.

The observations **made** show that the surface pressure fluctuations on the blade **s** are dominated by a **superposition of design properties, such as blade-tower distance and rotor tilt, which determine the blade-tower interaction** by a combination of the **rotor tilt, the blade-tower interaction**, and inflow properties, such as turbulence characteristic, **vertical wind shear** and flow inclination. **The inflow turbulence causes broadband fluctuations, the intensity of which is directly related to the turbulence characteristics.** **R3:G1-e** The changes in the angle of attack and the effective inflow velocity due to the rotor tilt causes the dominant pressure fluctuation at the rotation frequency. The amplitude of this fluctuation is amplified by the vertical wind shear as well as the inclined flow in the terrain. Fluctuations with higher harmonics of this frequency are triggered by the impulsive blade-tower interaction, independent of the inflow. However, the inflow turbulence causes broadband fluctuations, whose strength is directly related to the turbulence intensity, masking these harmonics. Therefore, it is **again** important to take the inflow into account realistically. **The impact of the blade-tower interaction on the blade is only slightly altered by the inflow, though.**

## 655 6 Conclusions

In this paper, results of a detailed turbine simulation coupled with an atmospheric code were presented to analyse the characteristics of blade-tower interactions as a cause of low-frequency noise emissions under complex terrain inflow. A highly resolved computational setup for a DDES of the complex terrain in Perdigião, including vegetation, has been established. Guidelines are given for dimensions and computational settings to obtain numerically stable results, and limitations in simulating valley flow are shown. A new workflow for the generating site and situation-specific inflow conditions using a steady atmospheric precursor simulation with *E-Wind* was presented. By calibrating this simulation with met-mast data, a real situation on 10 May

2017 was simulated and the flow field was investigated. A validation with met mast and lidar data showed that a site- and situation-specific flow field in Perdigão can be simulated well and with high accuracy using *FLOWer* as main solver, especially with respect to the local flow conditions at the turbine position.

665 The accurate simulation of the flow field around the turbine in Perdigão allows a realistic evaluation of the unsteady impact of the flow in complex terrain on surface pressure fluctuations on the turbine. Two reference simulations in flat terrain, one with uniform inflow and one with generic inflow turbulence, were performed to highlight differences. It was shown that turbulence as it occurs in the complex terrain in Perdigão massively alters the frequencies and position of strong surface pressure fluctuations caused by vortex shedding on the tower, also compared to turbulent inflow in flat terrain. This is due to the streamwise stretching of the turbulence in the inflow caused by the acceleration at the ridge and terrain characteristics. However, the dominance of the pressure fluctuations with the BPF and its higher harmonics at the upper tower section, caused by the blade-tower interaction, is not noticeably altered by the more realistic inflow. At the blade, on the other hand, the pressure fluctuations with multiples of the tower passage are masked by turbulent inflow, leaving the pressure fluctuations with the rotational frequency as the only discrete frequency in an otherwise broadband regime caused by the interaction of the blade with the inflow turbulence. The specific turbulence characteristics of the terrain flow have, however, no explicit effect on the pressure fluctuations on the blade compared to the generic turbulence in flat terrain, but the flow inclination counteracts shear and tilt effects.

**R3:G1-c** In this paper, the impact of turbulent inflow in complex terrain on surface pressure fluctuations on a turbine are investigated numerically using the hybrid RANS/LES flow solver *FLOWer*. A highly resolved computational setup for a DDES of a wind turbine in the complex terrain at Perdigão, including vegetation, is presented. A new workflow for the generation of site- and situation-specific inflow conditions using a steady-state atmospheric precursor simulation with *E-Wind* is introduced. The precursor simulation can be calibrated against met mast data, which is exemplified for a measured situation on 10 May 2017. The described CFD model provides numerically stable results of the global terrain flow, but shows limitations in simulation of the valley flow and increasing inaccuracy with the distance from the inlet. However, a validation with met mast and lidar data confirms that a site- and situation-specific flow field on the first ridge in Perdigão can be simulated well with the numerical process chain. Both mean velocities and turbulence up to 1 Hz are realistically captured at the turbine position. The generic turbine is included in the terrain simulation as a fully meshed structure and the CFD is coupled to a structural solver. Due to its aero-servo-elastic similarity with the commercial turbine, the findings are transferable to the real turbine erected at the site. The characteristics of the turbine wake can be compared with lidar measurements, for example, and are well represented in the simulation.

690 **R3:G1-c** The detailed simulation of the flow field around the turbine in Perdigão allows a realistic assessment of the impact of the flow in complex terrain on the surface pressure fluctuations on the turbine. Two reference simulations in flat terrain, one with uniform inflow and one with generic inflow turbulence, are performed to identify the terrain impact. It is shown that turbulent inflow alters the frequency and intensity of surface pressure fluctuations caused by vortex shedding at the tower, or more precisely, reduces their periodic pattern. However, the influence of turbulent inflow cannot be generalised. The terrain flow in Perdigão with its streamwise stretched turbulent structures (due to the acceleration at the ridge) causes different vortex shedding at the tower than turbulence in flat terrain. Nevertheless, the dominance of the periodic pressure fluctuations with

700 the BPF and its higher harmonics at the upper tower, caused by the blade-tower interaction, is not noticeably changed by the inflow. At the blade, however, the periodic pressure fluctuations with multiples of the tower passage, which are caused by the impulsive blade-tower interaction, are largely masked by the turbulent inflow. Only the pressure fluctuation with the rotational frequency remains as discrete frequency under turbulent inflow in the otherwise broadband regime. This is caused by a combination of rotor tilt, vertical wind shear and inclined flow, which again shows how important a realistic consideration of the inflow is.

705 In future studies, it is planned to post process the simulation results with a Ffowks-Williams-Hawking solver to evaluate the low-frequency acoustics ~~directly and to localise the main acoustic sources of low-frequency emissions on wind turbines~~. Subsequently, the most important acoustic sources for low-frequency emissions at wind turbines will be localised and compared with the areas found with high surface pressure fluctuations.

*Author contributions.* FW created the high-fidelity *FLOWer* setup, performed the CFD-MBS simulations, did the evaluation and wrote most of the paper. JL was responsible for the atmospheric *E-Wind* simulations and contributed the related parts of the paper. TL and EK initiated the research, supervised the work and revised the manuscript.

710 *Competing interests.* The authors declare that they have no conflict of interest.

*Acknowledgements.* The authors are very grateful to the German Federal Ministry for Economic Affairs and Energy (BMWi) for funding the research within the framework of the joint research projects Schall\_KoGe (FKZ 0324337C) and IndiAnaWind (FKZ 0325719F). The authors gratefully acknowledge the High-Performance Computing Center Stuttgart (HLRS) for providing computational resources within the project WEALoads.

## 715 References

- Adib, J., Langner, J., Alletto, M., Akbarzadeh, S., Kassem, H., and Steinfeld, G.: On the necessity of automatic calibration for CFD based wind resource assessment, <https://doi.org/10.13140/RG.2.2.19259.54560>, 2021.
- Alletto, M., Radi, A., Adib, J., Langner, J., Peralta, C., Altmikus, A., and Letzel, M.: E-Wind: Steady state CFD approach for stratified flows used for site assessment at Enercon, *Journal of Physics: Conference Series*, 1037, <https://doi.org/10.1088/1742-6596/1037/7/072020>,  
720 2018.
- Arnold, M., Wenz, F., Kühn, T., Lutz, T., and Altmikus, A.: Integration of system level CFD simulations into the development process of wind turbine prototypes, *Journal of Physics: Conference Series*, 1618, <https://doi.org/10.1088/1742-6596/1618/5/052007>, 2020.
- Batham, J.: Pressure distributions on circular cylinders at critical Reynolds numbers, *Journal of Fluid Mechanics*, 57, 209–228, <https://doi.org/10.1017/S0022112073001114>, 1973.
- 725 Bechmann, A. and Sørensen, N. N.: Hybrid RANS/LES method for wind flow over complex terrain, *Wind Energy*, 13, 36–50, <https://doi.org/10.1002/we.346>, <https://onlinelibrary.wiley.com/doi/10.1002/we.346>, 2010.
- Belcher, S. E. and Hunt, J. C.: Turbulent flow over hills and waves, *Annual Review of Fluid Mechanics*, 30, 507–538, <https://doi.org/10.1146/annurev.fluid.30.1.507>, 1998.
- Bruun, H. H. and Davies, P. O.: An experimental investigation of the unsteady pressure forces on a circular cylinder in a turbulent cross flow,  
730 *Journal of Sound and Vibration*, 40, 535–559, [https://doi.org/10.1016/S0022-460X\(75\)80062-9](https://doi.org/10.1016/S0022-460X(75)80062-9), 1975.
- Fernando, H. J., Mann, J., Palma, J. M., Lundquist, J. K., Barthelmie, R. J., Belo-Pereira, M., Brown, W. O., Chow, F. K., Gerz, T., Hocut, C. M., Klein, P. M., Leo, L. S., Matos, J. C., Oncley, S. P., Pryor, S. C., Bariteau, L., Bell, T. M., Bodini, N., Carney, M. B., Courtney, M. S., Creegan, E. D., Dimitrova, R., Gomes, S., Hagen, M., Hyde, J. O., Kigle, S., Krishnamurthy, R., Lopes, J. C., Mazzaro, L., Neher, J. M., Menke, R., Murphy, P., Oswald, L., Otarola-Bustos, S., Pattantyus, A. K., Veiga Rodrigues, C., Schady, A., Sirin, N.,  
735 Spuler, S., Svensson, E., Tomaszewski, J., Turner, D. D., Van Veen, L., Vasiljevic, N., Vassallo, D., Voss, S., Wildmann, N., and Wang, Y.: The Perdigao: Peering into microscale details of mountain winds, *Bulletin of the American Meteorological Society*, 100, 799–820, <https://doi.org/10.1175/BAMS-D-17-0227.1>, 2019.
- Gómez, A., Seume, J. R., and Hannover, D.: Load pulses on wind turbine structures caused by tower interference, *Wind Engineering*, 33, 555–570, <https://doi.org/10.1260/0309-524x.33.6.555>, 2009.
- 740 Gritskevich, M. S., Garbaruk, A. V., and Menter, F. R.: Fine-tuning of DDES and IDDES formulations to the  $k-\omega$  shear stress transport model, *Progress in Flight Physics*, 5, 23–42, <https://doi.org/10.1051/eucass/201305023>, 2013.
- Guma, G., Bangga, G., Lutz, T., and Krämer, E.: Aeroelastic analysis of wind turbines under turbulent inflow conditions, *Wind Energy Science*, 6, 93–110, <https://doi.org/10.5194/wes-6-93-2021>, 2021.
- Horvath, T. J., Jones, G. S., and Stainback, P. C.: Coherent shedding from a circular cylinder at critical, supercritical, and transcritical reynolds  
745 numbers, *SAE Technical Papers*, 95, 1123–1142, <https://doi.org/10.4271/861768>, 1986.
- IEC 61400-1: Wind turbines – Part 1: Design requirements, International Electrotechnical Commission, 2019.
- Johansson, J., Andersen, M. S., Christensen, S. S., Ingólfsson, K., and Karistensen, L. A.: Vortex Shedding from Tapered Cylinders at high Reynolds Numbers, in: 14th International conference on wind engineering, pp. 1–10, 2015.
- Jones Jr., G. W.: Unsteady lift forces generated by vortex shedding about a large, stationary, and oscillating cylinder at high Reynolds  
750 numbers, NASA Langley Research Center, 1968.

- Kim, Y., Weihing, P., Schulz, C., and Lutz, T.: Do turbulence models deteriorate solutions using a non-oscillatory scheme?, *Journal of Wind Engineering and Industrial Aerodynamics*, 156, 41–49, <https://doi.org/10.1016/j.jweia.2016.07.003>, 2016.
- Klein, L.: *Numerische Untersuchung aerodynamischer und aeroelastischer Wechselwirkungen und deren Einfluss auf tieffrequente Emissionen von Windkraftanlagen*, Verlag Dr. Hut, 2019.
- 755 Klein, L., Gude, J., Wenz, F., Lutz, T., and Krämer, E.: Advanced computational fluid dynamics (CFD)–multi-body simulation (MBS) coupling to assess low-frequency emissions from wind turbines, *Wind Energy Science*, 3, 713–728, <https://doi.org/10.5194/wes-3-713-2018>, 2018.
- Koblitz, T.: *CFD Modeling of non-neutral atmospheric boundary layer conditions*, PhD, DTU Wind Energy, 2013.
- Kowarsch, U., Keßler, M., and Krämer, E.: High order CFD-simulation of the rotor-fuselage interaction, in: *39th European Rotorcraft Forum*,  
760 Moscow, 2013.
- Kroll, N., Rossow, C. C., Becker, K., and Thiele, F.: The MEGAFLOW project, *Aerospace Science and Technology*, 4, 223–237, [https://doi.org/10.1016/S1270-9638\(00\)00131-0](https://doi.org/10.1016/S1270-9638(00)00131-0), 2000.
- Lalic, B. and Mihailovic, D. T.: An empirical relation describing leaf-area density inside the forest for environmental modeling, *Journal of Applied Meteorology*, 43, 641–645, [https://doi.org/10.1175/1520-0450\(2004\)043<0641:AERDLLD>2.0.CO;2](https://doi.org/10.1175/1520-0450(2004)043<0641:AERDLLD>2.0.CO;2), 2004.
- 765 Leschziner, M.: *Statistical turbulence modelling for fluid dynamics - Demystified*, Imperial College Press, <https://doi.org/10.1142/p997>, 2015.
- Letzgs, P., Lutz, T., and Krämer, E.: Detached eddy simulations of the local atmospheric flow field within a forested wind energy test site located in complex terrain, *Journal of Physics: Conference Series*, 1037, <https://doi.org/10.1088/1742-6596/1037/7/072043>, 2018.
- Luhmann, B., Seyedin, H., and Cheng, P. W.: Aero-structural dynamics of a flexible hub connection for load reduction on two-bladed wind  
770 turbines, *Wind Energy*, 20, 521–535, <https://doi.org/10.1002/we.2020>, 2017.
- Mann, J.: The Spatial Structure of Neutral Atmospheric Surface-Layer Turbulence, *Journal of Fluid Mechanics*, 273, 141–168, <https://doi.org/10.1017/S0022112094001886>, 1994.
- Mann, J.: Wind field simulation, *Probabilistic Engineering Mechanics*, 13, 269–282, [https://doi.org/10.1016/s0266-8920\(97\)00036-2](https://doi.org/10.1016/s0266-8920(97)00036-2), 1998.
- Mann, J., Angelou, N., Arnqvist, J., Callies, D., Cantero, E., Chávez Arroyo, R., Courtney, M., Cuxart, J., Dellwik, E., Gottschall, J., Ivanell,  
775 S., Kühn, P., Lea, G., Matos, J. C., Palma, J. M., Pauscher, L., Peña, A., Sanz Rodrigo, J., Söderberg, S., Vasiljevic, N., Veiga Rodrigues, C., Vasiljević, N., and Veiga Rodrigues, C.: Complex terrain experiments in the New European Wind Atlas, *Philosophical Transactions of the Royal Society A: Mathematical, Physical and Engineering Sciences*, 375, <https://doi.org/10.1098/rsta.2016.0101>, 2017.
- McCullough, G. B., Nitzberg, G. E., and Kelly, J. A.: *Preliminary investigation of the delay of turbulent flow separation by means of wedge-shaped bodies*, National Advisory Committee for Aeronautics, 1951.
- 780 Menke, R., Vasiljevic, N., and Mann, J.: DTU WindScanner lidar ridge scan data in NetCDF format. Version 1.0, <https://data.eol.ucar.edu/dataset/536.057>, Accessed: 14 Jun 2021, 2019a.
- Menke, R., Vasiljević, N., Wagner, J., Oncley, S., and Mann, J.: Multi-lidar wind resource mapping in complex terrain, *Wind Energy Science Discussions*, pp. 1–21, <https://doi.org/10.5194/wes-2019-85>, 2019b.
- Olsen, B. T.: *Mesoscale to microscale coupling for determining site conditions in complex terrain*, PhD, DTU,  
785 <https://doi.org/10.11581/00000036>, 2018.
- Palma, J. M., Silva, C. A., Gomes, V. C., Silva Lopes, A., Simões, T., Costa, P., and Batista, V. T.: The digital terrain model in the computational modelling of the flow over the Perdigão site: The appropriate grid size, *Wind Energy Science*, 5, 1469–1485, <https://doi.org/10.5194/wes-5-1469-2020>, 2020.

- Roache, P. J.: Perspective: A Method for Uniform Reporting of Grid Refinement Studies, *Journal of Fluid Engineering*, 116, 405–413, <https://doi.org/10.1115/1.2910291>, 1994.
- 790
- Rodríguez, I., Lehmkuhl, O., Chiva, J., Borrell, R., and Oliva, A.: On the flow past a circular cylinder from critical to super-critical Reynolds numbers: Wake topology and vortex shedding, *International Journal of Heat and Fluid Flow*, 55, 91–103, <https://doi.org/10.1016/j.ijheatfluidflow.2015.05.009>, 2015.
- Salim Dar, A., Berg, J., Troldborg, N., and Patton, E. G.: On the self-similarity of wind turbine wakes in a complex terrain using large eddy simulation, *Wind Energy Science*, 4, 633–644, <https://doi.org/10.5194/wes-4-633-2019>, 2019.
- 795
- Schulz, C., Klein, L., Weihing, P., and Lutz, T.: Investigations into the interaction of a wind turbine with atmospheric turbulence in complex terrain, *Journal of Physics: Conference Series*, 753, 032 016, <https://doi.org/10.1088/1742-6596/753/3/032016>, 2016.
- Shaw, R. H. and Schumann, U.: Large-eddy simulation of turbulent flow above and within a forest, *Boundary-Layer Meteorology*, 61, 47–64, <https://doi.org/10.1007/BF02033994>, 1992.
- 800
- Sogachev, A., Kelly, M., and Leclerc, M. Y.: Consistent two-equation closure modelling for atmospheric research: Buoyancy and vegetation implementations, *Boundary-Layer Meteorology*, 145, 307–327, <https://doi.org/10.1007/s10546-012-9726-5>, 2012.
- Sørensen, N. N. and Schreck, S.: Transitional DDES computations of the NREL phase-VI rotor in axial flow conditions, *Journal of Physics: Conference Series*, 555, <https://doi.org/10.1088/1742-6596/555/1/012096>, 2014.
- Spalart, P. R.: Young-Person’s guide to Detached-Eddy simulation grids, NASA Technical Note, 211032, 1003–1008, <http://dl.acm.org/citation.cfm?id=886734>, 2001.
- 805
- Spalart, P. R., Deck, S., Shur, M. L., Squires, K. D., Strelets, M. K., and Travin, A.: A new version of detached-eddy simulation, resistant to ambiguous grid densities, *Theoretical and Computational Fluid Dynamics*, 20, 181–195, <https://doi.org/10.1007/s00162-006-0015-0>, 2006.
- Troldborg, N., Sørensen, J. N., Mikkelsen, R., and Sørensen, N. N.: A simple atmospheric boundary layer model applied to large eddy simulations of wind turbine wakes, *Wind Energy*, 17, 657–669, <https://doi.org/10.1002/we.1608>, 2014.
- 810
- UCAR/NCAR: DLR Scanning Lidar Data Version 1.0, <https://data.eol.ucar.edu/dataset/536.060>, Accessed: 10 Aug 2020, 2019a.
- UCAR/NCAR: NCAR/EOL quality controlled high-rate ISFS surface flux data, geographic coordinate, tilt corrected. Version 1.1, <https://doi.org/10.26023/8X1N-TCT4-P50X>, 2019b.
- Vasiljević, N., Palma, J. M., Angelou, N., Matos, J. C., Menke, R., Lea, G., Mann, J., Courtney, M., Frölen Ribeiro, L., and Gomes, V. M.: Perdigaõ 2015: Methodology for atmospheric multi-Doppler lidar experiments, *Atmospheric Measurement Techniques*, 10, 3463–3483, <https://doi.org/10.5194/amt-10-3463-2017>, 2017.
- 815
- Vassberg, J. C., Tinoco, E. N., Mani, M., Brodersen, O. P., Eisfeld, B., Wahls, R. A., Morrison, J. H., Zickuhr, T., Laffin, K. R., and Mavriplis, D. J.: Abridged summary of the third AIAA computational fluid dynamics drag prediction workshop, *Journal of Aircraft*, 45, 781–798, <https://doi.org/10.2514/1.30572>, 2008.
- 820
- Wagner, J., Gerz, T., Wildmann, N., and Gramitzky, K.: Long-term simulation of the boundary layer flow over the double-ridge site during the Perdigaõ 2017 field campaign, *Atmospheric Chemistry and Physics*, 19, 1129–1146, <https://doi.org/10.5194/acp-19-1129-2019>, 2019.
- Weihing, P., Letzgus, J., Bangga, G., Lutz, T., and Krämer, E.: Hybrid RANS/LES capabilities of the flow solver FLOWer – Application to flow around wind turbines, in: *Progress in Hybrid RANS-LES Modelling*, pp. 369–380, Springer International Publishing, [https://doi.org/10.1007/978-3-319-70031-1\\_31](https://doi.org/10.1007/978-3-319-70031-1_31), 2018.

825 Wildmann, N., Kigle, S., and Gerz, T.: Coplanar lidar measurement of a single wind energy converter wake in distinct atmospheric stability regimes at the Perdigao 2017 experiment, *Journal of Physics: Conference Series*, 1037, <https://doi.org/10.1088/1742-6596/1037/5/052006>, 2018.

Yauwenas, Y.: Numerical simulation of blade-tower interaction noise, PhD, University of New South Wales, Australia, 2017.